

Satellite ice extent, sea surface temperature, and atmospheric methane trends in the Barents and Kara Seas

Ira Leifer¹, Robert Chen², Thomas McClimans³, and Frank Muller-Karger⁴

¹Bubbleology Research International

²University of South Florida

³SINTEF

⁴University of Southern Florida

November 22, 2022

Abstract

Large positive anomalies in lower troposphere methane (CH_4) in early fall of nearly every year (2003 to 2015) led to an average atmospheric CH_4 growth of 3.06 to 3.49 ppb yr^{-1} for the Barents and Kara Seas (BKS). At the same time, sea surface temperature (*SST*) increased from 0.0018 to 0.15 $^{\circ}\text{C yr}^{-1}$ while sea ice coverage decreased. Large positive CH_4 anomalies were discovered around Franz Josef Land (FJL) and offshore west Novaya Zemlya with smaller CH_4 enhancement and growth near Svalbard, downstream and north of known seabed CH_4 seepage. The strongest *SST* increase each year was in the southeast Barents Sea in June due to strengthening of the warm Murman Current (MC) and in the south Kara Sea in September. We propose that atmospheric CH_4 increase is occurring due to seepage from the petroleum reservoirs underlying the BKS and thawing of subsea permafrost and hydrates which then ventilates to the atmosphere from seasonal deepening of the surface ocean mixed layer and also from “methane shoaling” where currents transport deep water CH_4 into shallower waters. Continued strengthening heat transfer by the MC to the BKS will contribute to further warming (with the Barents Sea projected ice-free around 2030) and marine CH_4 emissions to the atmosphere.

Atmospheric methane, sea ice extent, and sea surface temperature trends (2003-2015) linked by oceanographic processes in the Barents and Kara Seas

Ira Leifer¹, F. Robert Chen², Thomas McClimans³, Frank Muller Karger², Leonid Yurganov⁴

¹ Bubbleology Research International, Inc., Solvang, CA, USA

² University of Southern Florida, USA

³ SINTEF Ocean, Trondheim, Norway

⁴ University of Maryland Baltimore County, Baltimore, USA (retired)

Correspondence to: Ira Leifer (ira.leifer@bubbleology.com)

Abstract Large positive anomalies in lower troposphere methane (CH_4) in early fall of nearly every year (2003 to 2015) led to an average atmospheric CH_4 growth of 3.06 to 3.49 ppb yr^{-1} for the Barents and Kara Seas (BKS). At the same time, sea surface temperature (*SST*) increased from 0.0018 to 0.15 $^{\circ}\text{C yr}^{-1}$ while sea ice coverage decreased. Large positive CH_4 anomalies were discovered around Franz Josef Land (FJL) and offshore west Novaya Zemlya with smaller CH_4 enhancement and growth near Svalbard, downstream and north of known seabed CH_4 seepage.

The strongest *SST* increase each year was in the southeast Barents Sea in June due to strengthening of the warm Murman Current (MC) and in the south Kara Sea in September. We propose that atmospheric CH_4 increase is occurring due to seepage from the petroleum reservoirs underlying the BKS and thawing of subsea permafrost and hydrates which then ventilates to the atmosphere from seasonal deepening of the surface ocean mixed layer and also from “methane shoaling” where currents transport deep water CH_4 into shallower waters. Continued strengthening heat transfer by the MC to the BKS will contribute to further warming (with the Barents Sea projected ice-free around 2030) and marine CH_4 emissions to the atmosphere.

Keywords: Arctic warming, marine methane emissions, sea surface temperature, sea ice, Barents and Kara Seas, mixed layer depth

Highlights:

- Current heat transport is driving increasing Barents and Kara Seas methane emissions.
- Winter deepening of the mixed layer and current shoaling are leading to growing methane emissions.
- Particularly strong CH_4 emissions were near Franz Josef Land and west of Novaya Zemlya.

36 1. Introduction

37 1.1 Changes in the Arctic Environment in the Anthropocene

38 Over recent decades the Arctic Ocean has been warming at nearly double the rate of the rest of the world’s oceans
 39 [O Hoegh-Guldberg and J F Bruno, 2010]. The strongest warming is for the Barents and Kara Seas (BKS) [S Lind
 40 et al., 2018] with Barents Sea waters warming from seabed to sea surface [S Watelet et al., 2020]. Associated is in-
 41 creasing Sea Surface Temperature (SST) and associated sea-ice reductions [R G Graversen et al., 2008; O Hoegh-
 42 Guldberg and J F Bruno, 2010; J C Stroeve et al., 2014].

43 Positive feedbacks underlie Arctic amplification; such as decreased sea-ice cover increasing solar insolation absorp-
 44 tion, thereby decreasing sea ice further, which also increases humidity and thus downwelling infrared radiation [J A
 45 Screen and I Simmonds, 2010]. Sea ice coverage relates to preceding ocean temperature anomalies, for example,
 46 Barents Sea winter ice relates to sea temperatures the prior winter-spring [P Schlichtholz, 2021]. As sea ice decreas-
 47 es, CH₄ flux to the atmosphere increases unimpeded [L N Yurganov et al., 2021], with additional atmospheric warm-
 48 ing. Another feedback involves deepening of the mixed layer due to ice-free winter cooling and wind mixing.

49 These feedbacks can be complex with some involving methane (CH₄). One feedback occurs from sea-ice reduction,
 50 which increases CH₄ flux to the atmosphere by no longer impeding gas transfer. Decreased stability can increase
 51 seabed CH₄ transport to the atmosphere by degrading the pycnocline and a Mixed Layer Depth (MLD) that reaches
 52 the bottom across much of the shallow BKS [Yurganov et al., 2021]. Another feedback involves decreased water-
 53 column stability from decreased sea ice from increased fresh water melt [S Lind et al., 2018]. Amplifying CH₄ emis-
 54 sions to the atmosphere are significantly slower winter than summer microbial oxidation rates [F Gründger et al.,
 55 2021]. Countering this amplification are likely lower winter seabed CH₄ emissions from subsea hydrate sources due
 56 to cooler winter bottom-water temperatures [B Ferré et al., 2020].

57 Arctic amplification has strong implications for CH₄ that is “sequestered” as subsea permafrost – terrestrial perma-
 58 frost inundated by rising sea levels after the Holocene. For example, extensive seabed CH₄ seepage is linked closely
 59 with destabilization of subsea permafrost in the East Siberian Sea [N Shakhova et al., 2013] with emissions estimat-
 60 ed as comparable to tundra emissions [N Shakhova et al., 2015]. Warmer seabed temperatures degrade subsea per-
 61 mafrost integrity [N Shakhova et al., 2017], enhancing emissions [N Shakhova et al., 2015]; however, timescales
 62 remain uncertain. Subsea permafrost is likely extensive in the Kara Sea, and possibly the southeast Barents Sea [T E
 63 Osterkamp, 2010]. Another feedback occurs from sea ice reduction, which increases CH₄ flux to the atmosphere by
 64 no longer impeding gas transfer.

65 The Arctic and sub-Arctic show strong terrestrial, high-latitude, positive CH₄ anomalies for eastern Canada, Alaska,
 66 and Western Russia (**Fig. 1**). Still, the strongest Arctic CH₄ anomalies by far are for the Barents Sea, which has the
 67 most rapid winter ice loss [I H Onarheim and M Årthun, 2017], and Kara Sea (**Fig. 1**). Yurganov et al. (2016) ana-
 68 lyzed IASI CH₄ seasonal anomalies below 4 km altitude for 2010-2015 and estimated Arctic marine CH₄ fluxes at
 69 ~2/3 Arctic terrestrial fluxes (north of 60° N). Yurganov et al. (2016) propose breakdown of the Arctic oceanic
 70 summer thermal stratification by wind-induced mixing in autumn may underlie this seasonal trend.

71 The study’s genesis was from a small-area scoping study in the marginal ice zone where Barents Sea water flows
 72 into the St. Anna Trough between Franz Josef Land and Novaya Zemlya (**Fig. 2b, star**). For these pixels, satellite
 73 SST and CH₄ (0-4 km) were correlated for one pixel population (**Fig. 3b**).

74 1.2. Study Motivation and Approach

75 We hypothesize that increases in water-column temperature drive subsea permafrost and hydrate destabilization that
 76 result in increased seabed CH₄ emissions, which manifests as increases in lower tropospheric CH₄, mediated by fall

deepening of the MLD and ventilation of deeper water CH₄. Our study area is the BKS, the Arctic hot spot for *SST* [Ø Skagseth et al., 2020] and CH₄ growth (**Fig. 1**). Currents are the major heat contributor to the Barents Sea on annual (Lien et al., 2013) and seasonal time-scales (Lien et al., 2017; Lien et al., 2013) and towards sea ice loss [M Årthun et al., 2019] with a 1-2.5 year residence time of Atlantic waters in the Barents Sea [L H Smedsrud et al., 2010].

The relationship between seabed CH₄ and atmospheric CH₄ is indirect, depending on water-column transport being faster than microbial oxidation, with CH₄ dissolved below the shallow summer pycnocline remaining trapped until winter storms extend the MLD to the seabed across most of the BKS. Thus, increasing current-driven heat input increases vertical transport across the water column, amplifying increasing seabed emissions.

Our study analyzed satellite *SST* and lower atmospheric CH₄ data for 2003-2015. Satellites cannot observe seabed temperatures; thus, *SST* is a proxy, albeit one where the seabed-*SST* connection is complex and is affected by processes including surface and sub-surface currents, meteorology, and solar insolation/long-wave downwelling radiation (i.e., cloudiness). The latter is avoided for cloud-cleared pixels. Still, *SST* follows dominant currents. Data were analyzed for statistically significant BKS trends relative to basin trends, which emphasizes localized processes (10s to 100s kms) and de-emphasizes basin-scale processes such as poleward atmospheric moisture transport that affect *SST* on basin scales. Trends are analyzed with respect to regional currents and winds to understand how their relationship to the spatial and temporal tropospheric CH₄.

We selected ten focus areas to test our hypothesis and evaluate differences in trends across the Barents Sea. Focus areas were large enough to allow pixel aggregation to decrease noise while small enough to avoid having spatial averaging reduce trends.

1.3 Sea surface temperature

SST is the ocean skin-layer temperature and depends on the balance between downwelling and upwelling (visible and thermal) radiation (modified by clouds and aerosols), heat transfer from the underlying ocean and overlying atmosphere and evaporative cooling (Frankignoul, 1985). Upper ocean wave mixing implies that persistent (multiple days) *SST* anomalies reflect ML temperature anomalies which are insulated by stratification from deeper water. Screen and Simmonds (2010) found the strongest Arctic warming is in the near-surface atmospheric layer and was most strongly related to sea ice retreat.

Solar insolation immediately affects *SST*, primarily from cloud cover changes, which cloud filtering removes on daily timescales. On longer timescales, changes in persistent cloudiness can cumulatively alter upper ocean temperatures (and *SST*). Increased cloudiness decreases incoming short wavelength radiation (cooling) while increasing long-wave radiation (warming) (Lee et al., 2017). However, these two effects largely counter each other with the balance further compensated by humidity and temperature profile changes (Schweiger et al., 2008). Given the canceling effects of persistent cloudiness and that significant changes in cloudiness are not observed outside areas of sea ice retreats, Screen and Simmonds (2010) conclude that “...changes in cloud cover have not contributed to recent [Arctic] warming.”

Currents and persistent winds create persistent *SST* anomalies. During summer, the warm BKS currents flow eastwards and northwards and are met by northerly winds from more northerly, cooler latitudes (Kolstad, 2008). This is the case in the fall for all of the Barents Sea except coastal Norway and Murman where winds track the currents and thus amplify warming (**Supp. Fig. S3**). The transition to north winds occurs offshore around the area of the Central Bank in the eastern Barents Sea. Fall winds in the north BKS are northerlies and thus cooling.

1.4 Global and Arctic Atmospheric Methane

Since pre-industrial times, CH₄ emissions have risen by a factor of 2.5 [E J Dlugokencky et al., 2011]. After stabilizing in the 1990s and early 2000s, CH₄ has resumed rapid growth since 2007, consistent with increases in FFI pro-

duction and associated CH₄ emissions [E G Nisbet et al., 2019], although other processes such as changing in hydroxyl (OH) loss may play a role [M Rigby et al., 2017]. Several processes may explain the CH₄ trend, including increasing emissions from the Arctic, wetlands, and fossil fuel, and/or decreasing losses from OH [M Saunio et al., 2020].

Global CH₄ concentrations increase poleward and are highest in the Arctic [X Xiong et al., 2016], driven by strong marine [N Shakhova et al., 2013] and terrestrial [M Saunio et al., 2020] CH₄ emissions. Arctic marine CH₄ arises from geologic seepage [N Shakhova et al., 2013], biogenic CH₄ production [R H James et al., 2016], hydrate decomposition [G K Westbrook et al., 2009], and submerged permafrost degradation [N Shakhova et al., 2013]. Also important is decreasing OH with latitude [Q Liang et al., 2017], enhancing Arctic winter CH₄ lifetime relative to lower latitudes. Arctic OH varies seasonally, imposing an ~10 ppb seasonality on Arctic CH₄ concentrations [T Thonat et al., 2017], whereas a seasonality of ~50 ppb in CH₄ is observed for the Zeppelin observatory on Svalbard [L Yurganov et al., 2016].

1.5. Airborne and Satellite Observations of Arctic Tropospheric Methane

Although the Arctic covers a vast territory, our knowledge of Arctic processes is highly limited both in spatial and seasonal coverage due to high cost and logistical challenges including the harshness of Arctic weather. Thus only a few airborne Arctic atmospheric campaigns have been conducted since 2005, reviewed in **Supp. Sec. S1**. Given the Arctic's vast spatial extent, measurement campaigns provide a few (typically summer) snapshots of a highly dynamic domain.

Satellite Arctic observations fill the significant existing temporal and spatial gaps between airborne and surface *in situ* datasets, particularly thermal infrared (TIR) CH₄ remote sensing, which uses spectral features at 7.82 μm [D M Tratt et al., 2014]. TIR sensors measure surface-emitted radiation day and night and can retrieve CH₄ above low clouds. TIR retrievals are more sensitive to mid-tropospheric CH₄ than near-surface CH₄ [X Xiong et al., 2013]. Details on the (InfraRed Atmospheric Sounder Interferometer) (IASI) and Atmospheric InfraRed Sounder (AIRS) TIR instruments and validation are presented in **Supp. Sec. S2**.

2. Method and Study Design

2.1. Methodology

2.1.1 Satellite data

CH₄ data (version 6) using a retrieval algorithm [B H Kahn et al., 2014; J Susskind et al., 2014] developed at the Goddard Space Flight Center (GSFC) for AIRS data since 2002 [AIRS Science Team/Joao Teixeira, 2016]. Data at https://acdisc.gesdisc.eosdis.nasa.gov/data/Aqua_AIRS_Level3/AIRX3SPM.006/. Data for both ascending and descending modes are analyzed for ocean areas with high vertical thermal contrast, *ThC*, defined as the temperature difference between the surface skin temperature and 4-km altitude air temperature. Only pixels with *ThC* > 10°C are considered [L Yurganov and I Leifer, 2016; L Yurganov et al., 2016] with CH₄ data re-projected to a 4-km azimuthal equal-area projection. The CH₄ anomaly (CH₄[']) is calculated by subtraction of the values computed within each focus area from the Barents Sea average each year. As CH₄ shows high inter-annual variability, a three-year running average is applied. CH₄ retrievals are accurate over both ice and seawater.

Ocean *SST* are from the Moderate Resolution Imaging Spectroradiometer (MODIS) sensor on the Aqua satellite, obtained from the GSFC, Ocean Ecology Laboratory, Ocean Biology Processing Group (OEL-OBPG). The 4-km, Level 3 data are re-projected to a 4-km, equal azimuthal area projection. Satellite data products are cloud screened [S Ackerman et al., 2010]. The mapped products match the CH₄ data projection. Cloud filtering removes pixels with partial cloud coverage, which would bias *SST* values.

First, data are quality reviewed for sea ice coverage and cloud coverage filtered for coastlines, which are from the Global Self-consistent, Hierarchical, High-resolution Shoreline database [SEADAS, 2017]. Shape files of sea-ice monthly extent are from the NSIDC (National Snow and Ice Data Center) [F Fetterer et al., 2017] and are based on monthly passive microwave radiometry from daily DMSP-SSMIS (Defense Meteorological Satellite Program – Special Sensor Microwave Imager/Sounder) data using a Bootstrap algorithm [J C Comiso et al., 2008]. Sea-ice fields are gridded on a polar stereographic grid at 25-km resolution. The number of ice-free months is derived from the intersection of the monthly ice shape file for each year with the focus areas. The number of ice-free months each year is tallied by the following rules: if the intersection is less than 15%, it is counted as 0 months; if coverage is greater than 15% and less than 50% of the pixel, it is counted as 0.5 months. When coverage is greater than 50% in a single month the pixel is counted as ice covered for the month. Ice-covered (>50%) pixels are not used in the SST trend analysis and mean values.

2.1.2 Trend analysis

To estimate trends, the monthly-mean time series for each grid point in the images covering this region are calculated. Then, a first-order polynomial is calculated by linear regression analysis. Linear trends are analyzed using the Mann Kendall Test [B Önöz and M Bayazit, 2003] and Sen’s linear trend analysis [H Juahir et al., 2010; P K Sen, 1968]. Visual analysis of the trends and anomaly maps of the Barents Sea were used to determine the focus areas’ locations. Focus area trends were calculated by averaging all valid (cloud cleared) pixels in each focus area for the same month for each year.

2.1.3 Focus Areas

The ten focus areas (**Fig. 4a**; **Supp. Table S1** for coordinates) were grouped into 5 oceanographic types, which are affected by (1) Arctic waters; (2) combined Arctic and Norwegian Atlantic Current; (3) Barents Sea Polar Front; (4) Murman Current; and (5) the Murman Coastal Current and Novaya Zemlya Current. The north easterly focus areas A1-A3 characterize the inflow of Arctic surface water through both gaps between the archipelagos of Svalbard and Franz Josef Land and between Franz Josef Land and Novaya Zemlya. Each exhibit different seasonal ice coverage. Another group of focus areas are west of Spitsbergen (A4-A6) and is influenced by the West Spitsbergen Current and water from the Barents Sea. Focus area A7 near Bear Island is affected by the warm, north-flowing east fork of the NAC and the cold, southwest-flowing Bear Island Current (BIC) and thereby is closest to the Barents Sea Polar Front region (Harris et al., 1998). Focus areas A8, A9, and A10 are influenced by the Murman Current and MCC with A9 situated in coastal waters offshore southwest Novaya Zemlya where ice coverage varies strongly seasonally. Focus areas can be classified in three larger groups, “Northwest of Barents” including the Greenland Sea and Fram Strait, west of Spitsbergen (A4-A6), “Northern Barents” in the marginal ice zone at the edge of the Arctic Basin (A1-A3) and “Southern Barents,” which is strongly influenced by heat from the east fork of the NAC (A7-A10). Note, focus areas A8 and A10 cover banks and A7 covers a shelf near Svalbard Bank.

3.0 Results

3.1. Barents and Kara Sea Oceanography and Meteorology

The relatively shallow (230-m average depth) Barents Sea is an adjacent sea to the Arctic Basin with complex bathymetry and hydrography [H Loeng, 1991]. (**Fig. 4b**). Currents are complex and important to Barents Sea oceanography (Fig. 4) and are dominated by inflow of warmer North Atlantic water through the Norwegian Atlantic Current (NAC), which forks into outflows along western Svalbard and through the Saint Anna Trough into the Arctic Ocean [H Loeng et al., 1997]. Cold Arctic water also flows into the Barents Sea through the Saint Anna Trough as the Percey Current (PC). See **Supp. Sec. S3** for details on BKS currents.

The Kara Sea is mostly shallow (< 50 m) and is controlled by the freshwater outflow of the Ob and Yenisei Rivers [L Polyak *et al.*, 2002], which largely drives overall surface currents northwards and causes the eastern Kara Sea to be brackish (Fig. 2b; Supp. Fig. S1). River inputs and flows between the Barents and Kara Seas also are important. Warmer water enters the south Kara Sea from the Barents Sea through the Kara Strait, joining a northward flowing slope current. Much of this water mixes with the south flowing, weak Novaya Zemlya Coastal Current (NZCC) returning to the Barents Sea through the Kara Strait [T A McClimans *et al.*, 1999; T A McClimans *et al.*, 2000].

Stratification plays an important role in the Barents Sea energy budget. Barents Sea water-column structure is modulated by winter cooling of surface waters and their convective mixing as well as brine rejection of seawater during ice formation. Winter vertical mixing extends to the seabed or near to the seabed over large portions of the shallow (200–300 m) Barents Sea [L N Yurganov *et al.*, 2021]. In spring, the warming of surface waters and freshwater from melting ice support water column stability and strengthens stratification in the central and southern Barents Sea [H Loeng, 1991]. Coastal waters off Norway and Murman remain stratified year-round due to terrestrial freshwater inputs [H Loeng, 1991].

Eastern Barents Sea winds generally circulate counterclockwise (cyclonically), strongly to the north along Novaya Zemlya in winter and weakly to the south in summer and fall [T Gammelsrød *et al.*, 2009]. This leads to calm winds over the Central Bank in fall and winter and generally weak easterlies near Franz Josef Land (fall to spring). Near Spitsbergen, winds are from the north year-round, weak in summer and strong in winter [E W Kolstad, 2008; G W K Moore, 2013]. The spring wind pattern is similar during winter, albeit displaced southwards and weaker. In summer, moderate winds (6 m s^{-1} average) blow from the north over most of the Barents Sea. Fall winds are similar to the summer, but stronger ($\sim 8\text{--}10 \text{ m s}^{-1}$) in the west (near Spitsbergen) and weaker in the east near Novaya Zemlya. Summer south Barents Sea winds are towards the north and later east near coastal Norway and Murman. The Barents Sea is stormy—winds are mostly southerly and above 15 m s^{-1} over 125 days annually [E W Kolstad, 2008]. In the east Barents Sea, winter winds transport more southerly, potentially warmer air, and in the summer winds from the southwest can transport warmer air along Norway and from the west along the Murman coasts; however, most of the Barents Sea most of the year experiences cold northerly winds. Moreover, much of the winter eastern Barents Sea is ice covered, insulating the sea from the air. Prevailing Kara Sea winds are mostly southwesterlies for the western Kara Sea and southerlies to southwesterlies for the central Kara Sea [A Kubryakov *et al.*, 2016]. See **Supp. Sec. S4** for further details on BKS winds.

Air temperatures on Bear Island have risen $\sim 1.7^\circ\text{C}$ since 1980 [V D Boitsov *et al.*, 2012], about triple the global atmospheric trend over the same period of $\sim 0.6^\circ\text{C}$ (<http://eca.knmi.nl/>) and about double the overall Arctic average [O Hoegh-Guldberg and J F Bruno, 2010]. For reference, temperatures in Murman have risen far faster at $0.12^\circ\text{C yr}^{-1}$ and $0.11^\circ\text{C yr}^{-1}$ in June and September 2002–2017, respectively (**Supp. Fig. S4**). These differences reflect that Bear Island is embedded in marine rather than coastal air and is influenced by the cold Bear Island Current.

3.2. Barents Sea *in situ* observations

In situ CH_4 transect measurements were made by cavity enhanced absorption spectroscopy (Los Gatos Research Inc., Mountainview, CA). Both transits followed a very similar trajectory (**Fig. 5b**; **Supp. Fig. S5**) that passed through focus areas A1 and A2. Very large, localized, CH_4 anomalies were observed. These anomalies were far off-shore and therefore not from distant terrestrial sources. The only reasonable explanation is seep bubble plumes reaching near the upper wave mixed layer or the sea surface; vessel exhaust was ruled out - see **Supp. Sec. S6** for more details.

CH_4 abruptly decreased around 72°N on the outwards transit, increasing again around 75°N . This depressed CH_4 portion of the transit was near where the vessel left the warm Murman Coastal Current (**Supp. Fig. S5b**). The strongest anomaly, to 100 ppb with concentrations to 2000 ppb, was observed on the southwards transit where the MCC rises over the sill into the Saint Anna Trough (78.7°N), close to Focus Area 8 (**Fig. 5**).

The two transits were separated by about a month with the September transit higher by ~30 ppb than in August, consistent with strong seasonal CH₄ changes. There were other significant differences. Whereas several narrow (and thus local) CH₄ anomalies were observed during the southwards transit, orders of magnitude more narrow anomalies were observed during the northwards transit. Also, the significant peak at 78.7°N only was observed during the southwards transit, indicating emissions variability.

The difference between these transits highlights the challenge of interpreting cruise “snapshot” data, with including comparing with satellite retrieval pixels. Specifically, data were compared with proximal IASI pixels that were within several days (**Supp. Fig. S6**). Agreement for the northwards transit was reasonably good (generally within 10 ppb) and generally poor for the southwards transit. Winter convection and vessel exhaust are ruled out.

3.3. Focused Study Area Annual Trends

Focus areas with the strongest decreasing ice cover trends (2003-2015) are in the marginal ice zone of the northern Barents Sea (south and southwest of Franz Josef Land) at the southern margin of the Arctic Basin (**Fig. 6a, A1-A3**). Trends for these three study areas are very similar (after classifying 2006 and 2014 for focus area A4 (Spitsbergen Northwest) as outliers). Note, focus areas A1-A3 show below-trend ice-free months in 2014 despite no significant 2014 SST deviation, supporting classification of 2014 as an outlier.

The similarity in ice coverage trends for area A3 (along the cold Percey Current) with areas A1 and A2 (along the Murman Current’s warm, northward leg) suggests not only increasing northward heat transfer, but also weakening southward cold-water advection. Area A4 (northwest of Spitsbergen) also shows decreasing ice coverage towards more frequent year-round ice-free status and lies at the Arctic Basin boundary (**Fig. 6b**), albeit more under the influence of warmer NAC waters than those under the influence of the Murman Current in the north-central Barents Sea (A1-A3). The Central Bank of the Barents Sea (**Fig. 6c, A10**) last saw an ice-covered month in 2005, while a noisy trend of decreasing ice coverage is evident offshore coastal southwest Novaya Zemlya (**Fig. 6c, A9**), along the western fork of the Murman Coastal Current. All focus areas trended towards year-round ice-free projecting year-round Barents ice free by ~2030.

SST increases in all focus areas, albeit at rates spanning a wide range from 0.0018 to 0.15 °C yr⁻¹ (**Fig. 6d-6f; Table 1**). In the Northern Barents Sea, the strongest warming trend is for area A1, south of Franz Josef Land. This is located in a marginal ice zone in the path of the warm MC. Area A3 shows the weakest warming trend lies along the cold Percey Current. For the Northwest of Barents focus areas (**Fig. 6e, A4-A6**), the strongest warming is at the northernmost focus area, A4, whereas the weakest trend is for the southernmost focus area (**Fig. 6d-6f, A6**). This is consistent with strengthened northwards penetration of the warm NAC and thus both the West Spitsbergen Current (WSC) and Bear Island Channel Current (BICC).

The strongest warming trend occurs southwest of Novaya Zemlya (**Fig. 6f, A9**) along the path of the northerly turn of the MCC, in shallow water. This trend is consistent with increased eastward MCC penetration along the west coast of Novaya Zemlya and into the Kara Sea. A very weak and highly variable SST warming trend is observed to the south of the Svalbard Bank at the intersection of the cold Percey Current with the warm NAC and BICC (A7). Areas A10 and A8, and to a lesser extent A9 all suggest a strong oscillation of ~8 years with peak values in 2005 – 2007, and a minimum around 2010. The same pattern also is observed to the south of Franz Josef Land (areas A1 and A2). All the boxes that exhibit this variability lie along the Murman Current, whose origin is in the NAC.

A positive CH₄ trend is observed across BKS with some regions exhibiting far stronger trends than average (**Fig. 6g-6i S7**). Areas of faster CH₄ increase include near Franz Josef Land (**Fig. 6g, A1, A2**), the shallower waters offshore W. Spitsbergen (**Fig. 6h, A4**), and offshore Novaya Zemlya (**Fig. 6i, A9**). These areas of increasing CH₄ correspond to areas of consistent warming for 2003-2015 (**Fig. 6d, A1, A2**) and consistent warming since ~2004/2005 for southwest offshore Novaya Zemlya and the Central Bank of the Barents Sea (**Fig. 6f, A8-A10**). All these focus areas lie along the northwards flow of the Murman Current and the Murman Coastal Current. The Central Bank also gets heat inflow from the BICC “warm core jet” [S Li and T A McCLimans, 1998]. Focus area A2 was crossed by the

in-situ transit and found CH₄ anomalies (**Fig. 5c**) best explained by CH₄ seepage. In contrast, focus areas along the Percey Current show a slowly decreasing CH₄ defined as relative to the entire Barents Sea trend (**Figs. 6g, 6i, A3, A7**), despite an (albeit weakly) increasing *SST*. Decreasing CH₄ for Spitsbergen WSW (**Fig. 6g-6i, A6**) could be associated with the cold East Greenland Current in the Fram Strait.

The strongest CH₄ growth is south of Franz Josef Land (**Table 1 A2**, 3.49 ppb yr⁻¹), followed by offshore northwest Spitsbergen (**Table 1 A4**, 3.37 ppb yr⁻¹ 2003-2015, 3.6 ppb yr⁻¹ 2005-2015). This positive trend is sustained over the analysis period. The area off the Fram Strait has natural CH₄ seepage associated with hydrate destabilization [*G K Westbrook et al.*, 2009]. This is an annual increase, and thus does not result from shifts in the timing of seasonal warming. Note, the CH₄ slopes for areas A4-A10 all are larger when calculated from the 2005 minimum, but not for A1-A3 (**Table 1**). The former lies along the NAC and its eastern current fork, the Murman Current. Neither the Percey Current focus areas (A3, A7) nor other northern Barents Sea focus areas (A1, A2) show this effect depending on the reference time.

The largest *SST* and CH₄ variability was in the focus area north of Murman in the Murman Current (MC) (**Table 1, A8; Fig. 6g-6i**), which likely arise from strength and course MC variations. *Ø Skagseth et al.* [2008] shows a nearly 50% variability in the volume flux through the Barents Sea Opening flux on decadal time-scales. Additional variability occurs from meteorology (and resultant change in cloudiness and hence solar insolation/downwelling radiation), and shifts in the location of the MC, which bifurcates around the focus area.

In general, CH₄ was at a low for most of the northwest Barents and southern Barents sites for the period 2004-2006 with an approximately 6-8 year cycle. *V D Boitsov et al.* [2012] shows seabed temperature variability for 2000-2009 and a suggested period of ~5-7 years, coolest in 2002-2005. This suggests a multiyear delay between seabed temperatures changes and CH₄ emission changes.

3.4. Climatology of the Barents and Kara Seas

The importance of currents is evident in the Barents Sea *SST* climatology where warm *SST* follows the warm currents (**Fig. 7; Supp. Fig. S3**). Warmer water flows eastward along the northern Norwegian and Murman coasts and offshore southeast of Spitsbergen along Svalbard Bank and then northward along the western Spitsbergen coast. In June, these flows correspond to “tendrils” of warmer water extending north to the east of the Central Bank and to the west of Novaya Zemlya and around Bear Island (and in September in the east Barents Sea. Water cools as it penetrates eastward and reaches the (seasonally-varying) ice edge. Across much of the Barents Sea there is a strong latitudinal *SST* gradient extending south from the ice edge, independent of the location of the eastern NAC branches. In the coastal waters of Novaya Zemlya, warmer water extends further north than elsewhere. The warm signature disappears in the area where the NAC submerges, near northwestern Novaya Zemlya.

In June, the edge of the cold (Arctic water) Percey Current/Bear Island Current (BIC) corresponds well with the warm water’s edge and also corresponds fairly well with the median ice edge location. Southeast of Spitsbergen, the BIC penetrates southward as a narrow extension of cold water ending south of Bear Island. Slightly cooler water is observed over the two banks in the central Barents Sea.

The shift to summer *SST* patterns occurs in July, increasing in August, and then beginning to decrease in September (**Supp. Fig. S7**). For Spitsbergen in the Svalbard archipelago (**Supp. Fig. S2**) the northerly cold Spitsbergen Coastal Current (SCC) inshore of the West Spitsbergen Current (WSC) breaks down. This suggests the SCC is entrained by the more energetic WSC (*Mcclimans*, 1994), flowing northwards underneath colder surface waters along southwest Spitsbergen, likely below strong summer stratification. The WSC flows farther offshore in June than in September, i.e., the Barents Front shifts shoreward in summer (**Supp. Fig. S3**).

September *SST* in the shallower eastern (coastal) Barents Sea has warmed to levels comparable to the warmer waters in the southwest Barents Sea where NAC heat input maintains elevated *SST*. Warmer *SST* also extends further offshore Norway and Murman. These seasonal *SST* changes match the sea ice’s northwards retreat to Franz Josef Land

(**Fig. 7b**) and shift of coastal winds to tailwinds over the currents. However, Barents Sea warming does not follow the ice edge between Svalbard and Franz Josef Land, corresponding instead to the front of the cold Percey Current. From August to September, the warm water has begun retreating across the Barents Sea with cold water associated with the Percey Current (**Supp. Fig. S7**).

The now mostly ice-free Kara Sea in September exhibits coastal warming, particularly to the east, where there also is heat input from the Ob and Yenisei Rivers (east of the Yamal Peninsula). This area exhibits warming despite partial ice coverage of the Gulf of Ob in June and likely is driven by warmer riverine water inputs.

CH₄ concentrations show a clear latitudinal trend that increases towards the north. This latitudinal gradient is weak in June and strong in September. Strong localized variations also occur in different Barents Sea regions. CH₄ concentrations along the Murman Current and in the (ice-covered) Kara Sea largely are below the latitudinal mean in June, whereas west of Spitsbergen and in the north-central Barents Sea they are above average.

In June, CH₄ is depressed strongly around Svalbard and around Franz Josef Land and Novaya Zemlya. For Spitsbergen, this corresponds to the cool SCC that hugs the shore. By September, CH₄ has shifted notably from depressed to the west of Novaya Zemlya (Novaya Zemlya Bank) to strongly enhanced CH₄ around the Franz Josef Land archipelago. Strong CH₄ enhancement also occurs in the outflow plumes of the Ob and Yenisei Rivers in the Kara Sea, around the Taymyr Peninsula. Around Svalbard, CH₄ rises to near latitudinal mean levels in September, except for offshore north Spitsbergen and Nordaustlandet (where sea ice remains).

3.5. Barents and Kara Seas trends

Across the Barents Sea, a number of different focus areas with distinct *SST* and CH₄ trends were identified (**Figs. 6**). These manifest significant spatial heterogeneity at the pixel scale and at the focus-area size scale. Thus, our analysis was applied to aggregated-pixel “focus areas” located in key regions where *SST* temporal and spatial changes are strongest (**Fig. 8**; **Supp. Fig. S8** for July and August trends).

June *SST* warming trends ($dSST/dt$) are fairly different from September *SST* trends (**Fig. 8**). In June, warming occurs much faster in the eastern Barents Sea, specifically, in waters affected by the Murman Coastal Current (MCC). Given that winds are from the north (**Supp. Fig. S3**) current-mediated heat transport opposes current warming. This suggests that the magnitude of atmospheric cooling during transit from the Atlantic is decreasing. Warming occurs primarily in shallow (generally less than 100-m deep) (**Fig. 8b**) waters that are generally well mixed. Sea ice is absent in this region by March-May, later in more northerly areas (**Fig. 4b**). Whereas there is no clear warming trend in July and August; a strong warming appears in the Kara Sea by September (**Supp. Fig. S8**), where winds also are cold northerlies. That this warming occurs several months after the ice retreat suggests that insolation is less important after the ice melts – the Kara Sea is ice-free in July (**Supp. Fig. S7**). This is consistent with increasing MCC penetration into the Kara Sea. *H Loeng* [1991] reported that MCC penetration into the Kara Sea was uncommon in the middle of the 20th century.

More rapid warming occurs offshore of the western coast of Novaya Zemlya from June-September. This is where the Murman Current (MC) transports water towards the St. Anna Trough (the dominant Barents Sea outflow), a region where shoaling is likely based on seabed topography (**Fig. 2b**). The MC then flows (and submerges under ice and Arctic surface water) along the east coast of Franz Josef Land. Enhanced warming is less near the northern margin of the Kara Sea, where river outflow dominates the oceanography.

Enhanced warming also occurs to the south and to the west-northwest of Svalbard in September, following approximately the trend of the northerly fork of the NAC. In contrast, waters off east Svalbard, where the East Spitsbergen Current (ESC) transports cold Arctic waters southwards, do not exhibit a significant warming trend in September, although it does exhibit warming in July. This suggests changes in the seasonal penetration of the PC into the Bar-

ents Sea, likely modulated by seasonal ice sheet retreat. There is no significant *SST* warming in June or September to the north of Franz Josef Land with ice-coverage persisting through September.

Overall Barents Sea atmospheric CH_4 is increasing (**Fig. 8C**), consistent with the global CH_4 trend (Nisbet et al., 2014). However, it is notable that some regions exhibit significantly more rapidly increasing CH_4 than the global or Barents Sea trends. In June, CH_4 trends ($d\text{CH}_4'/dt$) are largely similar in both ice-free and ice-covered areas. In near-coastal waters around Svalbard (except the east), in northern Norwegian fjords, and for the White Sea (Murmansk) where CH_4 growth is enhanced.

September $d\text{CH}_4'/dt$ (when ice coverage has retreated to the northern edge of the Barents Sea and Kara Sea - **Fig. 8b**) are strongly enhanced in the east Barents Sea and the south Kara Sea. These areas coincide with areas of enhanced *SST* warming and show CH_4' trends almost three times as high as the general Arctic trend. Moreover, they are under northerly winds and thus terrestrial sources cannot contribute (**Supp. Fig. S3**). In contrast, regions without enhanced warming, particularly waters affected by cold currents, exhibit the weakest CH_4' growth. Also, CH_4' increases strongly in the Kara Strait between the Barents and Kara Seas, an area where methane shoaling is likely.

Enhanced CH_4' growth is not evident in June or September to the north of Spitsbergen, despite strong *SST* increases; however, significant increases are evident here in August. This follows significant CH_4 enhancement in July to the southeast of Spitsbergen. This July-August shift follows the NAC.

3.6. Barents and Kara Seas oil and gas reservoirs

The Barents and Kara seas contain significant and extensive oil and gas reserves, which in the case of the Russian Kanin Peninsula extend onshore where they are produced and transported by pipeline (**Fig. 9**). Additional extensive proven hydrocarbon resources are found in the shallow southwest Kara Sea [L Rise et al., 2015]. These reservoirs correspond to the paths of the Murman and Murman Coastal currents, providing potential sources of CH_4 to these waters that then is transported towards the Barents Seas outflows. There is good correspondence between these hydrocarbon reservoirs (proven and potential) with areas of fast CH_4 growth and areas of likely methane shoaling. Given the relationship between major river outflows and hydrocarbon reserves globally (e.g., the Mississippi, the Amazon, the Congo, the Nile) that similar reserves underlie the shallow northeastern Kara Sea.

4. Discussion

4.1. Seabed-atmosphere methane transport

There are a number of mechanisms that allow seabed CH_4 emissions to reach the sea surface, both due to direct bubble-mediated transport and by turbulence (from bubble-dissolved CH_4). Transport is bubble-mediated because the microbial filter blocks aqueous CH_4 migration through near seabed sediments [W S Reeburgh, 2014]. Rising bubbles lose CH_4 to the water column by dissolution, transporting the remainder with larger bubbles losing less gas than smaller bubbles. In shallow water seep bubbles directly transport most CH_4 to the sea surface [I Leifer and R Patro, 2002]. For example, numerical modelling of field data by I Leifer et al. [2017] found ~25% of Laptev Sea seabed CH_4 from 70 m reached the atmosphere by bubbles.

4.1.1. Storm sparging of the mixed layer depth is faster than microbial oxidation

The dissolved CH_4 's fate depends on timescales of vertical mixing versus microbial oxidation. Microbial oxidation timescales are days to weeks in plumes extending to decadal where concentrations approach ambient [W S Reeburgh, 2014]. Storm-induced mixing timescales are short for the shallow, summer mixed layer (50-70 m) In winter, the MLD extends to the seabed for most of the BKS [L N Yurganov et al., 2021]. Thus, turbulence transport in stormy arctic seas is more efficient than microbial oxidation given that winds are above 15 m s^{-1} for over 125 days per year [E W Kolstad, 2008]. In practical terms, bubble transport to the MLD means that seepage extends the effective CH_4 MLD by 50-100 m to 150-300 m in the winter, covering most of the BKS (**Fig. 2b**).

This highlights the importance of seasonal stratification, which storms breakdown [I Leifer *et al.*, 2015], efficiently sparging dissolved MLD CH₄ to the atmosphere [N Shakhova *et al.*, 2013]. Seasonally, the pycnocline collapse from fall storms releases CH₄ sequestered between the summer MLD and winter MLD [J Nauw *et al.*, 2015; L N Yurganov *et al.*, 2021], though there are summer microbial oxidation losses of this dissolved CH₄ [F Gründger *et al.*, 2021]. Also important is thermal convection mixing which reaches the seabed in northeastern Barents Sea and elsewhere [T A McClimans and J H Nilsen, 1993]. Nonetheless, S Watelet *et al.* [2020] shows increasing temperatures across the water column, including near-seafloor temperatures. Seabed temperatures have increased at 0.05 - 0.06 °C per year [L N Yurganov *et al.*, 2021].

A key exception to the summer sequestration of CH₄ below the MLD occurs where currents drive waters upslope into the MLD - methane shoaling. Methane shoaling is discussed in **Sec. 4.3**

4.1.2. Potential for oily emissions

The above discussion was for non-oily seepage. However, where seepage arises from a petroleum hydrocarbon reservoir, bubbles likely are oily. Oil slows bubble rise [I Leifer, 2010] and dramatically reduces dissolution, allowing their survival far higher in the water column than non-oily bubbles [I Leifer and I MacDonald, 2003]. Oily bubbles can reach the sea surface from the deep sea – e.g., I R MacDonald *et al.* [2010] tracked seep bubbles by remote operated vehicle from 1 km depth to the WML and found a significant positive CH₄ anomaly in surface waters. Given the presence of extensive proven and proposed petroleum reservoirs across the Barents and Kara Seas [P Rekacewicz, 2005], some Barents Sea seepage is likely oily with enhanced CH₄ transport to the sea surface. *In situ* data (**Fig. 5**) showed localized strong atmospheric CH₄ plumes above deep water that are best explained by oily bubbles. These plumes were above areas of confirmed oil and gas deposits within an extensive region of potential oil and gas deposits in the central and northern Barents Sea (**Fig. 9**). Thus, *in situ* data suggest more extensive oil deposits than currently confirmed deposits. Oil slick observations would provide confirmation, but require calm winds.

4.1.3 Non-Barents and Kara Seas methane sources

One unlikely source of BKS CH₄ anomalies is atmospheric transport as there is neither significant local industry nor extensive wetlands/terrestrial permafrost nearby or upwind for the prevailing wind directions. Prevailing winds are from the north in June and September except for south and southeast Barents Sea where winds track the coast and the NCC and MCC in September. Note—synoptic systems can transport CH₄ from northern Europe or Russia to the Barents Sea, but synoptic system winds are not dominant (prevailing) and thus play a small role in time-averaged datasets. Moreover, these terrestrial sources are distant, implying large size scale anomalies, which would decrease with distance from northern Europe. Instead, the anomalies are localized and decrease towards Europe. Additionally, *in situ* data show highly localized anomalies (**Fig. 5**). The one case where September winds could transport terrestrial CH₄ into the marine atmosphere is from oil production and pipeline infrastructure from the Kanin and Yamal Peninsulas near Kolguyev Island (**Fig. 9**). However, extensive CH₄ plumes (**Fig. 9**) are not observed in coastal and near coastal pixels (except the east Kara Sea, particularly the Ob and Yenisei Rivers), and dCH_4/dt trends (**Fig. 8**) were not lower than those further offshore.

4.2. Hydrocarbon reserves and local atmospheric methane

Seabed seepage, often thermogenic (petroleum hydrocarbon), is identified in all oceans and all petroleum-producing basins [A Judd and M Hovland, 2007] and likely plays a role in BKS CH₄ anomalies. In the Kara Sea, the correlation of enhanced CH₄ with depth is poor, which is shallower to the north. Instead, the location of enhanced September CH₄ closely matches the location of oil and gas reserves, e.g., **Fig. 9**; P Rekacewicz [2005], and also the Murman Coastal Current's path of warm water as it follows the coastline of the Kanin Peninsula and then enters the Kara Sea.

Although there is extensive oil and gas production on the Yamal Peninsula, prevailing winds blow away from the Barents Sea. Note, the trend shows enhanced CH₄ growth, implying increasing emissions, i.e., not steady-state seabed warming but increased seabed warming. This increasing CH₄ growth is for September, not June, corresponding to when the water column is warmest in the South Barents Sea [J E Stiansen *et al.*, 2009]. Also, the Barents Sea outflow through Saint Anna's Trough is greater in September (about double) than June [T Gammelsrød *et al.*, 2009] when the growth in the CH₄ anomaly occurs (**Fig. 6**). The importance of this transport also is apparent in the SST trend with the greatest warming occurring in June in the southeast Barents Sea (offshore the Kanin Peninsula) near the Kara Strait. This region lies to the west of the areas of enhanced CH₄ growth in September near the Kara Strait. In contrast, significant SST warming is not observed in September in this easternmost region of the Barents Sea.

Two other areas of enhanced CH₄ growth lie in the north-central Barents Sea, north of Central Bank, and offshore northern Novaya Zemlya. These regions lie along the Murman Current and over the Central Bank – a region where the MC and the BICC “warm core jet” converge. Water flowing in this direction also is forced upwards – from 300-400 m to just 100 m as it crosses a sill into the St. Anna Trough with rising seabed towards the east and towards Novaya Zemlya with water depths of just tens of meters (**Fig. 2b**). Additionally, this region of increasing CH₄ growth corresponds spatially to the potential (i.e., unproven) gas and oil reserves that extend across the Saint Anna Trough to Franz Josef Land, e.g., **Fig. 9**; P Rekacewicz [2005]. There also are proven oil and gas fields to the south, also along the Murman Current's path, but south of the area of increasing CH₄ offshore northwest Novaya Zemlya. These hydrocarbon fields also correlate with increasing CH₄ trends offshore southwest Novaya Zemlya.

4.3. Methane Shoaling Hypothesis

Where CH₄-rich currents shoal, they vertically transport dissolved CH₄ into shallow waters where it can diffuse to the atmosphere. *Methane shoaling* allows seabed CH₄ to reach the atmosphere distant from its seabed source, typically beyond the reach of in situ studies, but covered in satellite data – even beyond political boundaries. Even microbial oxidation CH₄ rates in plumes order several weeks [W S Reeburgh, 2014] allows horizontal transport order 100-1000 km.

Methane shoaling is the best explanation for the localized, strong and growing, atmospheric BKS CH₄ anomalies, specifically the Kara Straits and along the Novaya Zemlya coast near Central Bank. Areas of enhanced CH₄ growth were closely related to the path of the Murman Coastal Current as it flows towards the Kara Strait rather than seabed depth (**Fig. 9**). Both the rising seabed bathymetry and the presence of both southwards and northwards currents through the Kara Strait imply strong vertical mixing and shoaling. Along the Murman Current path significant petroleum hydrocarbon reservoirs that likely release seep CH₄ into Murman Current waters.

Further methane shoaling evidence is from the dCH₄/dt spatial distribution around Kolguyev Island (north of the White Sea), which increased faster on its western side than its eastern side, even though the seabed to the island's east is shallower. In fact, the CH₄ spatial pattern correlates better with shadowing in the island's lee from shoaling currents, rather than with seabed depth. Prevailing winds are from the south-southeast [A Kubryakov *et al.*, 2016], thus atmospheric transport cannot explain the pattern.

Notably, the enhanced CH₄ concentrations around Franz Josef Land does not correlate with the location of potential hydrocarbon reserves, but does correlate with depth and the flow of the Murman Current, also consistent with methane shoaling. Although some of the enhanced CH₄ growth near Novaya Zemlya could arise from increasing local seabed emissions, seabed temperatures were below zero until 2009 [V D Boitsov *et al.*, 2012]. This would imply submerged hydrate deposits remain largely undegraded.

4.4. Sea surface temperature

The analysis shows CH₄ anomaly growth (dCH_4/dt) that implies strengthening seabed sources if atmospheric conditions remain constant. Specifically, dCH_4/dt over portions of the BKS is faster than the Barents Sea mean and the latitudinal mean. To some level these correlate with enhanced SST warming, but the correlation is poor. SST is the

skin temperature and depends on radiative balance, atmospheric temperature (including transport and latent heat) and heat transfer from the bulk ocean. Another factor underlying this poor correlation is that there is a delay between *SST* warming and ocean-column warming of several months [J E Stiansen *et al.*, 2009]. There also appears to be a several year response time; the ~6-8 year variability is suggestive of an oscillation in the *SST* trend in the Southern Barents Sea (areas A8, A9, and A10) and has a very similar timescale to the seabed trends reported by V D Boitsov *et al.* [2012], albeit preceding it by ~2-4 years.

More rapid *SST* warming occurs offshore Novaya Zemlya moving northwards from June-September, where the Murman Current transports water and the seabed topography is likely to cause shoaling. This suggests that warmer terrestrial weather is not driving Kara Sea changes as this would occur uniformly both in the south Kara Sea, which is influenced by the Barents Sea, and the northern Kara Sea, which is influenced by river outflow. Additionally, if increased riverine heat input were driving the trend, the greatest enhancement would be in the northern Kara Sea, which also is shallower.

There are several hypotheses for why *SST* is warming fastest in Murman Current and NAC waters. One is sea-ice retreat; however, the warming occurs several months after the sea ice retreat. Another is that the mixed layer is becoming shallower, allowing more rapid cooling to the atmosphere. This would imply a weakening of storms and winds – which firstly is inconsistent with warmer *SST*, and secondly, there is no indication that Barents Sea storminess is changing or progressing further northwards [T Koyama *et al.*, 2017]. Cloudiness changes affect *SST*; however, pixel cloud filtering removes this effect, whereas persistent cloudiness changes largely cancel outside of areas of sea ice retreat [A J Schweiger *et al.*, 2008].

Another hypothesis is that increasing ocean current heat transport is driving the *SST* warming. Although *SST* derives from several factors including heat transfer from the bulk ocean (i.e., currents), its co-spatial relationship to enhanced CH₄ anomaly is consistent with currents playing a major role both at the sea surface (*SST* anomaly trend) and at the seabed. This supports using *SST* as a surrogate for water column temperature. Greater heat transport could occur from strengthening and/or warming currents.

Seabed September temperatures [N Shakhova *et al.*, 2013] do not suggest increased warmer seabed temperatures north of Norway and Russia, but do suggest warmer seabed temperatures to the east and also along Novaya Zemlya – suggesting a greater importance of the MC. This is consistent with the model of T A McClimans *et al.* [2000] that current advection of ice shift the marginal ice zone’s location. The warming trend suggests a strengthening of the seasonal trend in the Barents Sea outflow, which is greater in September than June [T Gammelsrød *et al.*, 2009].

The most rapid warming is for the shallow water off northwest Svalbard (area A4) (**Fig. 6**), which also exhibited the strongest CH₄ growth. In this area, seabed topography is nearly flat over an extensive shelf with depths in the range 250-400 m. Where the shelf falls off sharply, rising sea temperatures will minimally induce hydrate destabilization. In contrast, where the shelf falls off very gently, small temperature increases shift extensive areas of seabed from below to above the hydrate stability field. This area is immediately to the north of the area where several researchers have identified extensive seabed seep CH₄ emissions, which raised aqueous CH₄ concentration, but did not significantly reach the atmosphere in the area significantly [S Mau *et al.*, 2017; C L Myhre *et al.*, 2016; G K Westbrook *et al.*, 2009]. The most likely explanation is a strengthening of the West Spitsbergen Current and changes in the Barents Sea Polar Front. Notably, these Svalbard area CH₄ anomalies are smaller than those off Novaya Zemlya and Franz Joseph Land. These emissions are beyond the BKS and this study’s scope - for further discussion, see **Supp. Sec. S8** are beyond the scope of this paper and area

4.5. Ice-free Barents Sea

The southern Barents Sea has been ice free since at least 1850 [J E Walsh *et al.*, 2016]. Meanwhile the northwest Barents Sea is near ice-free year-round, whereas northeast Barents Sea (around Franz Josef Land and St. Anna Trough) remains ice-covered for about six months (**Fig. 6**). The ice coverage trends suggest most of the Barents Sea will be ice free, year-round circa 2030. This is comparable to the 2023-2036 estimate of I H Onarheim and M

Årthun [2017; Fig. 3], which also notes that the current decreasing trend lies outside the oscillation envelope since 1850. Ice records since 1850 show fairly stable sea ice through 1980 in March (within $\pm 20\%$), and 1970 in September (within $\pm 50\%$), decreasing to date [J E Walsh et al., 2016]. For the Barents Sea, and other marginal Arctic seas most significant ice loss occurs in late summer [I H Onarheim et al., 2018].

The Barents Sea is a marginal sea between the temperate Norwegian Sea and the Arctic Basin and thus is the conduit through which lower-latitude oceanic heat is transmitted to the Arctic Basin [I H Onarheim and M Årthun, 2017]. Given the significant role the Barents Sea plays in overall Arctic ice loss - fully 25% of the loss is attributed to the Barents Sea, which comprises 4% of the Arctic Ocean including marginal seas [L H Smedsrud et al., 2013], implications will be significant for weather at lower latitudes, and the marine ecosystem. Seemingly counter-intuitive, sea ice reduction increases the upwards surface heat flux as ice has an insulating effect. Thus ice-loss somewhat stabilizes Arctic Basin ice, particularly during winter [I H Onarheim and M Årthun, 2017] and may even lead to growth of ice in the Arctic Basin and northern Greenland Sea. Still, the data herein are consistent with a progressive weakening of the Percey Current, which will continue to cause ice loss off east Svalbard and warming of these waters. This agrees with M A Alexander et al. [2004] who concluded that the (semi-stationary due to bathymetry) Barents Sea Polar Front has shifted due to the domination of Atlantic over Arctic waters.

As noted, the progression of ice loss in the south and east Barents Sea along the pathway of the Murman Coastal Current has led to a progressive loss of ice in the south Kara Sea. Thus, the balance between the two processes - heat loss to the atmosphere and heat gain by currents to the Kara Sea are clearly shifting towards warmer. The implications of decreasing ice cover in the shallow Kara Sea are significant with respect to CH₄ emissions - the area is rich in hydrocarbon resources that currently are sequestered under submerged permafrost that will continue to degrade, while warming seabed temperatures will enhance microbial degradation of the vast organic material deposited over the millennia by the Ob and Yenisei Rivers. Thus, the already significant importance of Arctic CH₄ anomaly from the Kara Sea will accelerate due to feedbacks from an ice-free Barents Sea.

5. Conclusion

In this study, the global, repeat nature of satellite data was used to investigate the relationship between currents, and trends in sea surface temperature, ice extent, and methane (CH₄) anomaly for the Barents and Kara Seas for 2003-2015. Large positive CH₄ anomalies were discovered around Franz Josef Land and offshore west Novaya Zemlya in September, in areas with downstream current shoaling, with far smaller CH₄ enhancement around Svalbard, again, strongest where currents likely shoal down-current of seabed seepage. This highlights a major strength of satellite data: Identification of sources that are not part of an apriori used to initialize inversion models.

The strongest SST growth was southeast Barents Sea in June where strengthening of the warm Murman Current (an extension of the Norwegian Atlantic Current) could explain the trend, and in the south Kara Sea in September, whereas the cold southwards-flowing Percey Current weakened. These regions also exhibit the strongest CH₄ growth enhancement as well as around Franz Josef Land. Likely sources are CH₄ seepage from extensive oil and gas reservoirs underlying the central and east Barents Sea and Kara Sea; however, the spatial pattern was poorly correlated with depth and best correlated with strengthened currents that shoal.

Trends in the Barents Sea and Kara Seas suggest an ice-free Barents Sea free in around 2030, while driving seabed warming and enhanced CH₄ emissions, particularly from areas where currents drive methane shoaling. Methane shoaling certainly is important in other marine settings, although timescales likely vary for other basins.

Data availability. All data needed to evaluate the conclusions in the paper are present in the paper and/or the Supplementary Materials and are publicly available from governmental servers identified in the Methods section.

Competing interests. The authors declare that they have no conflict of interest.

Author contributions: IL Developed the study, analyzed data, made figures, and wrote and edited the manuscript. RC analyzed data and made figures, and reviewed the manuscript, TC edited the manuscript, FMK participated in developing the study, and edited the manuscript, LY, participated in developing the study, analyzed data, made figures, and wrote and edited the manuscript.

Acknowledgements: The research was supported by a grant from NASA ROSES2013: “A.28, The Science of TERRA AND AQUA: Long-term Satellite Data Fusion Observations of Arctic Ice Cover and Methane as a Climate Change Feedback.” We thank Vladimir Ivanov, Arctic and Antarctic Research Institute, for organizing the NABOS cruise and Cathrine Lund Myrhe, Norwegian Air Research Institute (NILU), for calibration gas used during the NABOS cruise.

Financial Support. This work was supported by a grant from the NASA Earth Science Division.

References

- Ackerman, S., K. Strabala, P. Menzel, R. A. Frey, C. Moeller, and L. E. Gumley (2010), Discriminating clear-sky from cloud with {MODIS}, Algorithm Theoretical Basis Document (MOD35)Rep. ATB-MOD-06, 129 pp.
- AIRS Science Team/Joao Teixeira (2016), AIRS2RET: AIRS/Aqua L2 Standard Physical Retrieval (AIRS-only) V006, edited, Goddard Earth Sciences Data and Information Services Center (GES DISC), Greenbelt, MD.
- Alexander, M. A., U. S. Bhatt, J. E. Walsh, M. S. Timlin, J. S. Miller, and J. D. Scott (2004), The atmospheric response to realistic Arctic sea ice anomalies in an AGCM during winter, *Journal of Climate*, 17(5), 890-905.
- Årthun, M., T. Eldevik, and L. H. Smedsrud (2019), The role of Atlantic heat transport in future Arctic winter sea ice loss, *Journal of Climate*, 32(11), 3327-3341.
- Bøe, R., et al. (2015), Sandwaves and sand transport on the Barents Sea continental slope offshore northern Norway, *Marine and Petroleum Geology*, 60, 34-53.
- Boitsov, V. D., A. L. Karsakov, and A. G. Trofimov (2012), Atlantic water temperature and climate in the Barents Sea, 2000–2009, *ICES Journal of Marine Science*, 69(5), 833-840.
- Comiso, J. C., C. L. Parkinson, R. Gersten, and L. Stock (2008), Accelerated decline in the Arctic sea ice cover, *Geophysical Research Letters*, 35(1), L01703.
- Dlugokencky, E. J., E. G. Nisbet, R. Fisher, and D. Lowry (2011), Global atmospheric methane: Budget, changes and dangers, *Philosophical Transactions of the Royal Society A: Mathematical, Physical and Engineering Sciences*, 369(1943), 2058-2072.
- Ferré, B., et al. (2020), Reduced methane seepage from Arctic sediments during cold bottom-water conditions, *Nature Geoscience*, 13, 144-148.
- Fetterer, F., K. Knowles, W. Meier, M. Savoie, and A. K. Windnagel (2017), Sea Ice Index (version 3), edited, National Snow and Ice Data Center (NSDIC), Boulder, CO.
- Gammelsrød, T., Ø. Leikvin, V. Lien, W. P. Budgell, H. Loeng, and W. Maslowski (2009), Mass and heat transports in the NE Barents Sea: Observations and models, *Journal of Marine Systems*, 75(1-2), 56-69.
- Graversen, R. G., T. Mauritsen, M. Tjernstrom, E. Kallen, and G. Svensson (2008), Vertical structure of recent Arctic warming, *Nature*, 451(7174), 53-56.
- Gründger, F., D. Probandt, K. Knittel, V. Carrier, D. Kalenitchenko, A. Silyakova, P. Serov, B. Ferre, M. Svenning, and H. Niemann (2021), Seasonal shifts of microbial methane oxidation in Arctic shelf waters above gas seeps, *Limnology and Oceanography*, 66, 1-19.
- Hoegh-Guldberg, O., and J. F. Bruno (2010), The impact of climate change on the world's marine ecosystems, *Science*, 328(5985), 1523-1528.
- Jakobsson, M., et al. (2012), The International Bathymetric Chart of the Arctic Ocean (IBCAO) Version 3.0, *Geophysical Research Letters*, 39(12), L12609.
- James, R. H., et al. (2016), Effects of climate change on methane emissions from seafloor sediments in the Arctic Ocean: A review, *Limnology and Oceanography*, 61, 5281-5299.
- Juahir, H., S. M. Zain, A. Z. Aris, M. K. Yusof, M. A. A. Samah, and M. B. Mokhtar (2010), Hydrological trend analysis due to land use changes at Langat River Basin, *Environment Asia*, 3, 20-31.
- Judd, A., and M. Hovland (2007), *Seabed fluid flow: The impact on geology, biology and the marine environment*, 492 pp., Cambridge University Press, Cambridge, UK.
- Kahn, B. H., et al. (2014), The Atmospheric Infrared Sounder version 6 cloud products, *Atmospheric Chemistry and Physics*, 14(1), 399-426.
- Kolstad, E. W. (2008), A QuikSCAT climatology of ocean surface winds in the Nordic seas: Identification of features and comparison with the NCEP/NCAR reanalysis, *Journal of Geophysical Research: Atmospheres*, 113(D11), D11106.

- Koyama, T., J. Stroeve, J. Cassano, and A. Crawford (2017), Sea ice loss and Arctic cyclone activity from 1979 to 2014, *Journal of Climate*, 30(12), 4735-4754.
- Kubryakov, A., S. Stanichny, and A. Zatsepin (2016), River plume dynamics in the Kara Sea from altimetry-based Lagrangian model, satellite salinity and chlorophyll data, *Remote Sensing of Environment*, 176, 177-187.
- Leifer, I. (2010), Characteristics and scaling of bubble plumes from marine hydrocarbon seepage in the Coal Oil Point seep field, *Journal Geophysical Research*, 115(C11), C11014.
- Leifer, I., and R. Patro (2002), The bubble mechanism for methane transport from the shallow seabed to the surface: A review and sensitivity study, *Continental Shelf Research*, 22(16), 2409-2428.
- Leifer, I., and I. MacDonald (2003), Dynamics of the gas flux from shallow gas hydrate deposits: interaction between oily hydrate bubbles and the oceanic environment, *Earth and Planetary Science Letters*, 210(3-4), 411-424.
- Leifer, I., D. Chernykh, N. Shakhova, and I. Semiletov (2017), Sonar gas flux estimation by bubbleinsonification: Application to methane bubble flux from seep areas in the outer Laptev Sea, *The Cryosphere*, 11(3), 1333-1350.
- Leifer, I., E. Solomon, J. Schneider v. Deimling, R. Coffin, G. Rehder, and P. Linke (2015), The fate of bubbles in a large, intense bubble plume for stratified and unstratified water: Numerical simulations of 22/4b expedition field data, *Journal of Marine and Petroleum Geology*, 68B, 806-823.
- Li, S., and T. A. McClimans (1998), The effects of winds over a barotropic retrograde slope current, *Continental Shelf Research*, 18(5), 457-485.
- Liang, Q., et al. (2017), Deriving global OH abundance and atmospheric lifetimes for long-lived gases: A search for CH₃CCl₃ alternatives, *Journal of Geophysical Research: Atmospheres*, 122(21), 11,914-911,933.
- Lind, S., R. B. Ingvaldsen, and T. Furevik (2018), Arctic warming hotspot in the northern Barents Sea linked to declining sea-ice import, *Nature Climate Change*, 8(7), 634-639.
- Loeng, H. (1991), Features of the physical oceanographic conditions of the Barents Sea, *Polar Research*, 10(1), 5-18.
- Loeng, H., V. Ozhigin, and B. Ådlandsvik (1997), Water fluxes through the Barents Sea, *ICES Journal of Marine Science*, 54(3), 310-317.
- MacDonald, I. R., O. Garcia-Pineda, J. Chanton, M. Kastner, E. Solomon, I. Leifer, T. Naehr, S. Yvon-Lewis, and K. John (2010), HYFLUX: Remote sensing and sea truth of CH₄ flux from the Gulf of Mexico seep system, paper presented at 10th International Conference on Gas in Marine Sediments, Lake Baikal, Russia, 6-12 Sept. 2010.
- Mau, S., et al. (2017), Widespread methane seepage along the continental margin off Svalbard - from Bjørnøya to Kongsfjorden, *Scientific Reports*, 7, 42997.
- McClimans, T. A., and J. H. Nilsen (1993), Laboratory simulation of the ocean currents in the Barents sea, *Dynamics of Atmospheres and Oceans*, 19(1), 3-25.
- McClimans, T. A., B. O. Johannessen, and J. H. Nilsen (1999), Laboratory simulation of fronts between the various water masses in the Kara Sea, paper presented at Oceanic Fronts and Related Phenomena (Konstantin Federov Memorial Symposium), Intergovernmental Oceanographic Commission (IOC) Workshop Report, UNESCO'99, Pushkin, St. Petersburg, Russia.
- McClimans, T. A., D. R. Johnson, M. Krosshavn, S. E. King, J. Carroll, and Ø. Grenness (2000), Transport processes in the Kara Sea, *Journal of Geophysical Research: Oceans*, 105(C6), 14121-14139.
- Moore, G. W. K. (2013), The Novaya Zemlya Bora and its impact on Barents Sea air-sea interaction, *Geophysical Research Letters*, 40(13), 3462-3467.
- Myhre, C. L., et al. (2016), Extensive release of methane from Arctic seabed west of Svalbard during summer 2014 does not influence the atmosphere, *Geophysical Research Letters*, 43(9), 2016GL068999.

711 Nauw, J., P. Linke, and I. Leifer (2015), Bubble momentum plume as a possible mechanism for an early
 712 breakdown of the seasonal stratification in the northern North Sea, *Journal of Marine and Petroleum*
 713 *Geology*, 68, 789-805.
 714 Nisbet, E. G., et al. (2019), Very strong atmospheric methane growth in the 4 years 2014–2017:
 715 Implications for the Paris Agreement, *Global Biogeochemical Cycles*, 33(3), 318-342.
 716 Onarheim, I. H., and M. Årthun (2017), Toward an ice-free Barents Sea, *Geophysical Research Letters*,
 717 44, 8387-8395.
 718 Onarheim, I. H., T. Eldevik, L. H. Smedsrud, and J. C. Stroeve (2018), Seasonal and regional
 719 manifestation of Arctic Sea ice loss, *Journal of Climate*, 31(12), 4917-4932.
 720 Önöz, B., and M. Bayazit (2003), The power of statistical tests for trend detection, *Turkish Journal of*
 721 *Engineering and Environmental Sciences*, 27(4), 247-251.
 722 Osterkamp, T. E. (2010), Subsea Permafrost, in *Climate and Oceans*, edited by J. H. Steele, S. A. Thorpe
 723 and K. K. Turekian, pp. 252-264, Academic Press, London UK.
 724 Ozhigin, V. K., R. B. Ingvaldsen, H. Loeng, V. D. Boitsov, and A. L. Karsakov (2011), The Barents Sea,
 725 in *The Barents Sea - ecosystem, resources, management. Half a century of Russian - Norwegian*
 726 *cooperation*, edited by T. Jakobsen and V. K. Ozhigin, pp. 38-76, Tapir Academic Press, Trondheim,
 727 Norway.
 728 Polyak, L., S. Korsun, L. A. Febo, V. Stanovoy, T. Khusid, M. Hald, B. E. Paulsen, and D. J. Lubinski
 729 (2002), Benthic foraminiferal assemblages from the Souterhn Kara Sea - A river-influenced Arctic
 730 marine environment, *The Journal of Foraminiferal Research*, 32(3), 252-273.
 731 Reeburgh, W. S. (2014), Global Methane Biogeochemistry, in *Treatise on Geochemistry (Second*
 732 *Edition)*, edited by R. Keeling, pp. 71-94, Elsevier-Pergamon, Oxford.
 733 Rekacewicz, P. (2005), Oil and gas development and seabirds colonies in the Barents Region, in
 734 *Barentswatch Atlas*, edited, UNEP/GRIDA-Arendal.
 735 Rigby, M., et al. (2017), Role of atmospheric oxidation in recent methane growth, *Proceedings of the*
 736 *National Academy of Sciences*, 114(21), 5373-5377.
 737 Rise, L., V. K. Bellec, S. Chand, and R. Bøe (2015), Pockmarks in the southwestern Barents Sea and
 738 Finnmark fjords, *Norwegian Journal of Geology*, 94(4), 263-282.
 739 Saunio, M., et al. (2020), The global methane budget 2000-2017, *Earth System Science Data*, 12(3),
 740 1561-1623.
 741 Schlichtholz, P. (2021), Relationships between wintertime sea ice cover in the Barents Sea and ocean
 742 temperature anomalies in the era of satellite observations, *Journal of Climate*, 34(5), 1565-1586.
 743 Schweiger, A. J., R. W. Lindsay, S. Vavrus, and J. A. Francis (2008), Relationships between Arctic Sea
 744 ice and clouds during autumn, *Journal of Climate*, 21(18), 4799-4810.
 745 Screen, J. A., and I. Simmonds (2010), The central role of diminishing sea ice in recent Arctic
 746 temperature amplification, *Nature*, 464(7293), 1334-1337.
 747 SEADAS (2017), edited.
 748 Sen, P. K. (1968), Estimates of the regression coefficient based on Kendall's tau, *Journal of the American*
 749 *Statistical Association*, 63(324), 1379-1389.
 750 Shakhova, N., et al. (2013), Ebullition and storm-induced methane release from the East Siberian Arctic
 751 Shelf, *Nature Geoscience*, 7, 64-70.
 752 Shakhova, N., et al. (2015), The East Siberian Arctic Shelf: Towards further assessment of permafrost-
 753 related methane fluxes and role of sea ice, *Philosophical Transactions of the Royal Society A:*
 754 *Mathematical, Physical and Engineering Sciences*, 373(2052), 1-13.
 755 Shakhova, N., et al. (2017), Current rates and mechanisms of subsea permafrost degradation in the East
 756 Siberian Arctic Shelf, *Nature Communications*, 8, 15872.
 757 Skagseth, Ø., T. Eldevik, M. Årthun, H. Asbjørnsen, V. S. Lien, and L. H. Smedsrud (2020), Reduced
 758 efficiency of the Barents Sea cooling machine, *Nature Climate Change*, 10(7), 661-666.
 759 Skagseth, Ø., T. Furevik, R. Ingvaldsen, H. Loeng, K. A. Mork, K. A. Orvik, and V. Ozhigin (2008),
 760 Volume and heat transports to the Arctic Ocean via the Norwegian and Barents Seas, in *Arctic–*

- 761 *Subarctic Ocean Fluxes: Defining the Role of the Northern Seas in Climate*, edited by R. R. Dickson,
762 J. Meincke and P. Rhines, pp. 45-64, Springer Netherlands, Dordrecht.
- 763 Smedsrud, L. H., R. Ingvaldsen, J. E. Ø. Nilsen, and Ø. Skagseth (2010), Heat in the Barents Sea:
764 Transport, storage, and surface flux, *Ocean Science*, 6, 219-234.
- 765 Smedsrud, L. H., et al. (2013), The role of the Barents Sea in the Arctic climate system, *Reviews of*
766 *Geophysics*, 51(3), 415-449.
- 767 Stiansen, J. E., O. Korneev, O. Titov, P. Arneberg, A. Filin, J. R. Hansen, Å. Høines, and S. Marasaev
768 (2009), Joint Norwegian-Russian environmental status 2008. Report on the Barents Sea Ecosystem.
769 Part II – Complete report *Rep. 1502-8828*, 375 pp, Norwegian Marine Data Center (NMDC).
- 770 Stiansen, J. E., et al. (2006), Joint PINRO/IMR report on the state of the Barents Sea ecosystem
771 2005/2006(3/2006), 122.
- 772 Stroeve, J. C., T. Markus, L. Boisvert, J. Miller, and A. Barrett (2014), Changes in Arctic melt season and
773 implications for sea ice loss, *Geophysical Research Letters*, 41(4), 1216-1225.
- 774 Susskind, J., J. M. Blaisdell, and L. Iredell (2014), *Improved methodology for surface and atmospheric*
775 *soundings, error estimates, and quality control procedures: the atmospheric infrared sounder science*
776 *team version-6 retrieval algorithm*, 1-34, 34 pp., SPIE.
- 777 Thonat, T., et al. (2017), Detectability of Arctic methane sources at six sites performing continuous
778 atmospheric measurements, *Atmospheric Chemistry and Physics*, 17(13), 8371-8394.
- 779 Tratt, D. M., K. N. Buckland, J. L. Hall, P. D. Johnson, E. R. Keim, I. Leifer, K. Westberg, and S. J.
780 Young (2014), Airborne visualization and quantification of discrete methane sources in the
781 environment, *Remote Sensing of Environment*, 154, 74-88.
- 782 Walsh, J. E., F. Fetterer, J. Scott Stewart, and W. L. Chapman (2016), A database for depicting Arctic sea
783 ice variations back to 1850, *Geographical Review*, 107(1), 89-107.
- 784 Watelet, S., Ø. Skagseth, V. S. Lien, H. Sagen, Ø. Østensen, V. Ivshin, and J. M. Beckers (2020), A
785 volumetric census of the Barents Sea in a changing climate, *Earth System Science Data*, 12(4), 2447-
786 2457.
- 787 Westbrook, G. K., et al. (2009), Escape of methane gas from the seabed along the West Spitsbergen
788 continental margin, *Geophysical Research Letters*, 36.
- 789 Xiong, X., Y. Han, Q. Liu, and F. Weng (2016), Comparison of atmospheric methane retrievals from
790 AIRS and IASI, *IEEE Journal of Selected Topics in Applied Earth Observations and Remote Sensing*,
791 9(7), 3297-3303.
- 792 Xiong, X., C. Barnet, E. S. Maddy, A. Gambacorta, T. S. King, and S. C. Wofsy (2013), Mid-upper
793 tropospheric methane retrieval from IASI and its validation, *Atmospheric Measurement Techniques*,
794 6(9), 2255-2265.
- 795 Yurganov, L., and I. Leifer (2016), Estimates of methane emission rates from some Arctic and sub-Arctic
796 areas based on orbital interferometer IASI data, *Current Problems in Remote Sensing of Earth from*
797 *Space (Sovremennye Problemy Distantzionnogo Zondirovaniya Zemli iz Kosmosa)*, 13(2), 173-183.
- 798 Yurganov, L., I. Leifer, and C. Lund-Myhre (2016), Seasonal and interannual variability of atmospheric
799 methane over Arctic Ocean from satellite data, *Current Problems in Remote Sensing of Earth from*
800 *Space (Sovremennye Problemy Distantzionnogo Zondirovaniya Zemli iz Kosmosa)*, 13(2), 107-119.
- 801 Yurganov, L. N., D. Carrol, A. Pnyushkov, I. Polyakov, V., and H. Zhang (2021), Ocean stratification
802 and sea-ice cover in Barents and Kara seas modulate sea-air methane flux: Satellite data, *Advances in*
803 *Polar Science*, 32(2), 118-140.

TABLES

Table 1. Slopes of *SST* ($^{\circ}\text{C yr}^{-1}$), CH_4' (ppb yr^{-1}), and CH_4' (ppb yr^{-1}) for focus boxes. ^a

Box	<i>SST</i>	CH_4'	CH_4'	CH_4' (Barents) ^b	CH_4' (Arctic) ^c
	2003-2015	2003-2015	2005-2015	2003-2015	2003-2015
A1	0.102	3.35	3.26	0.179	0.0750
A2	0.0319	3.49	3.38	0.267	0.213
A3	0.00178	3.19	3.17	-0.0185	0.00574
A4	0.0867	3.37	3.60	0.310	0.391
A5	0.0279	3.10	3.22	0.0105	0.0319
A6	0.00259	3.07	3.24	-0.0123	0.0548
A7	0.0323	3.06	3.27	-0.0460	-0.119
A8	0.0552	3.11	3.35	0.0642	-0.0544
A9	0.145	3.20	3.44	0.103	0.109
A10	0.0527	3.32	3.51	0.122	0.0613

^a *SST* – Sea Surface Temperature, CH_4' – methane anomaly.

^b CH_4' relative to the Barents Sea

^c CH_4' relative to the Arctic Ocean

FIGURE CAPTIONS

Figure 1 Arctic and sub-arctic annual methane (CH_4), 0.5° gridded, 0-4 km altitude, 2016, from Infrared Atmospheric Sounding Interferometer (IASI-A); mountainous regions blanked. Data were filtered as in Yurganov and Leifer (2016a). Data key on panel. For polar stereographic view see **Supp. Fig. S9** and Supplemental Movie of entire time series.

Figure 2 a) Arctic map, showing study area (Blue Square) and average January and September 2003-2015 ice extent. **b)** Bathymetry of the study area (87.468 N, 1.219E; 72.056N, 0.173E; 63.008N, 48.05E; 69.707N, 82.793E) from Jakobsson et al. (2012). Dashed black line shows approximate Barents Sea boundaries. Dashed white line shows edge of submerged permafrost from Osterkamp (2010). Star shows scoping study pixels location. Depth data key on panel.

Figure 3. Comparison of the sea surface temperature (SST) and methane (CH_4) for 2003-2015 for pixels between Franz Josef Land and Novaya Zemlya (**Fig. 2b, Star, Supp. Table 1, Box A2**). Red diamonds show SST and CH_4 averages within the study area. Blue and green ovals highlight pixels with different CH_4 trends for SST (all CH_4), and ($\text{CH}_4 > 1925$ ppb), respectively.

Figure 4. a) Simplified currents for Barents and nearby seas, bathymetry features, and focus-area boxes. Green, red, and blue arrows are coastal, warm Atlantic origin, and cold polar currents, respectively. Broken lines illustrate current subduction. Bathymetry from *M Jakobsson et al.* [2012]. **b)** Monthly ice extent for 2015. Focus study boxes (numbered); see **Supp. Table S1** for coordinates. Arrow points to North Pole. Barents Sea currents adapted from *J E Stiansen et al.* [2006]; for near Svalbard from *H Loeng* [1991]; see **Supp. Fig. S2** for greater detail for Svalbard area; for Kara Sea area from *L Polyak et al.* [2002]; see **Supp. Fig. S1** for greater detail. For Barents Sea Opening area from *R Bøe et al.* [2015]. East Barents Sea Currents from *V K Ozhigin et al.* [2011]

Figure 5. Surface *in situ* methane (CH_4) on the *R/V Akademik Fyodorov* for Barents Sea **a)** northwards transect for 21 Aug. 2013. Focus areas along pathway shown. **b)** Southwards transect for 17-22 Sept. 2013. Also shown is the 300-m depth contour and edges of the Murman Coastal Current, from PINRO (http://www.pinro.ru/labs/hid/kolsec1_e.htm). Note, Data key on figure. **c)** CH_4 profiles during northerly and southerly transits, labeled.

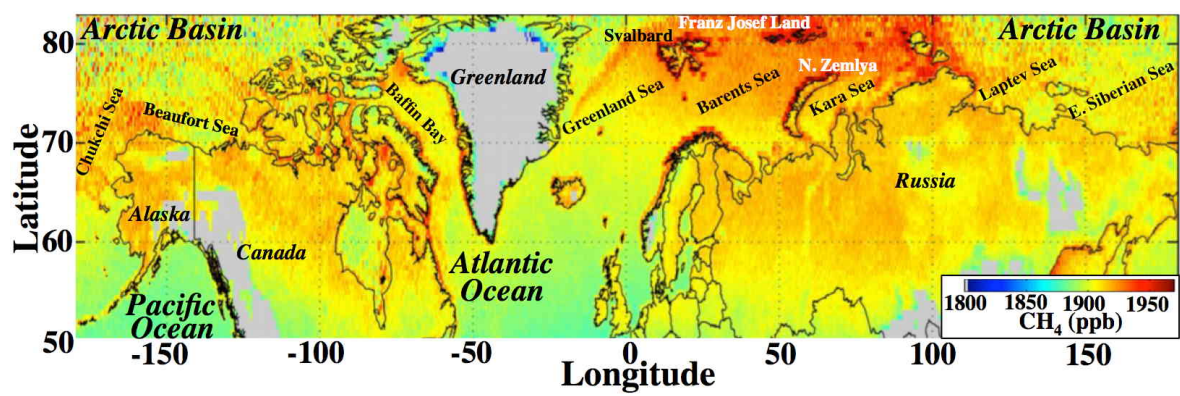
Figure 6. Focus study area time series for 2003-2015 for **a-c)** Ice-free months, labeled on figure, **d-f)** sea surface temperature (SST). Annual values are average of all months, generally May-October, which are ice-free, **g-i)** methane (CH_4). Annual data and 3 year, rolling-average data shown. Anomaly is relative to entire Barents Sea. Data key and focus area names on figure. See **Fig. 4a** and **Supp. Table S1** for locations.

Figure 7. Mean values for 2003 to 2015 of sea surface temperature (SST) for **a)** June and **b)** September. Mean methane (CH_4) concentration for **c)** June and **d)** September. Median ice edge for

same period is shown. Years with reduced ice extent contribute to values of *SST* north of this ice edge. Data key on figure. See **Supp. Fig. S3** for overlay of currents.

Figure 8. Linear trends for 2003 to 2015 of sea surface temperature ($dSST/dt$) for **a)** June and **b)** September. Methane concentration trend (dCH_4/dt) for **c)** June and **d)** September. ND – not detectable – failed statistical test. Blue, black dashed lines show 100 and 50 m contour, respectively. Data key on figure.

Figure 9. Barents Sea location of oil and gas fields and potential fields, and pipelines. Also shown are the approximate locations of the major Barents Sea currents – the Murman Current (MC), Murman Coastal Current (MCC), Bear Island Current (BIC), and Percey Current (PC). Areas outlined in red are where $dCH_4/dt > 3$ ppb yr⁻¹ from **Fig. 6i**. Adapted from *P Rekacewicz* [2005].



879

880 **Figure 1.** Arctic and sub-arctic annual methane (CH₄), 0.5° gridded, 0-4 km altitude, 2016, from
881 Infrared Atmospheric Sounding Interferometer (IASI-A); mountainous regions blanked. Data
882 were filtered as in Yurganov and Leifer (2016a). Data key on panel. For polar stereographic view
883 see **Supp. Fig. S9** and Supplemental Movie of entire time series.
884

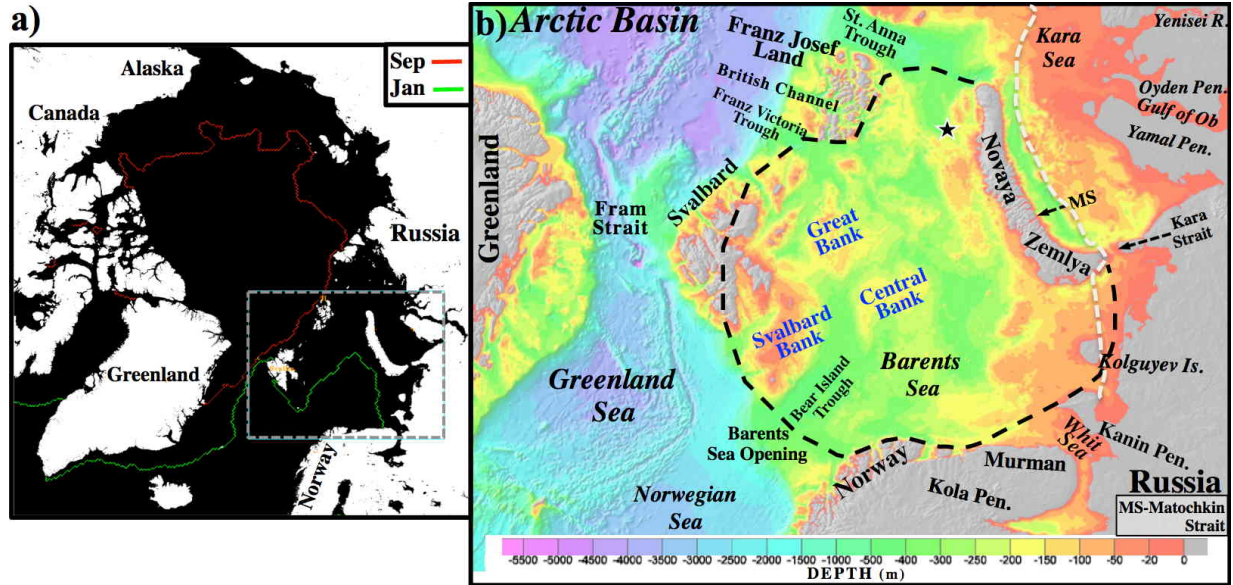


Figure 2. a) Arctic map, showing study area (Blue Square) and average January and September 2003-2015 ice extent. **b)** Bathymetry of the study area (87.468 N, 1.219E; 72.056N, 0.173E; 63.008N, 48.05E; 69.707N, 82.793E) from Jakobsson et al. (2012). Dashed black line shows approximate Barents Sea boundaries. Dashed white line shows edge of submerged permafrost from Osterkamp (2010). Star shows scoping study pixels location. Depth data key on panel.

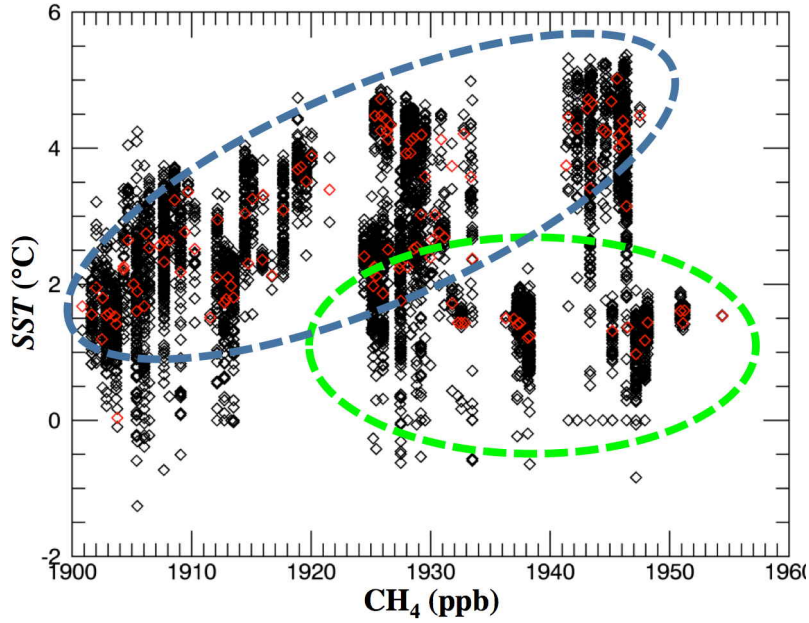


Figure 3. Comparison of the sea surface temperature (*SST*) and methane (CH_4) for 2003-2015 for pixels between Franz Josef Land and Novaya Zemlya (**Fig. 2b, Star, Supp. Table 1, Box A2**). Red diamonds show monthly *SST* and CH_4 averages within the study area. Blue and green ovals highlight pixels with different CH_4 trends for *SST* (all CH_4), and ($\text{CH}_4 > 1925$ ppb), respectively.

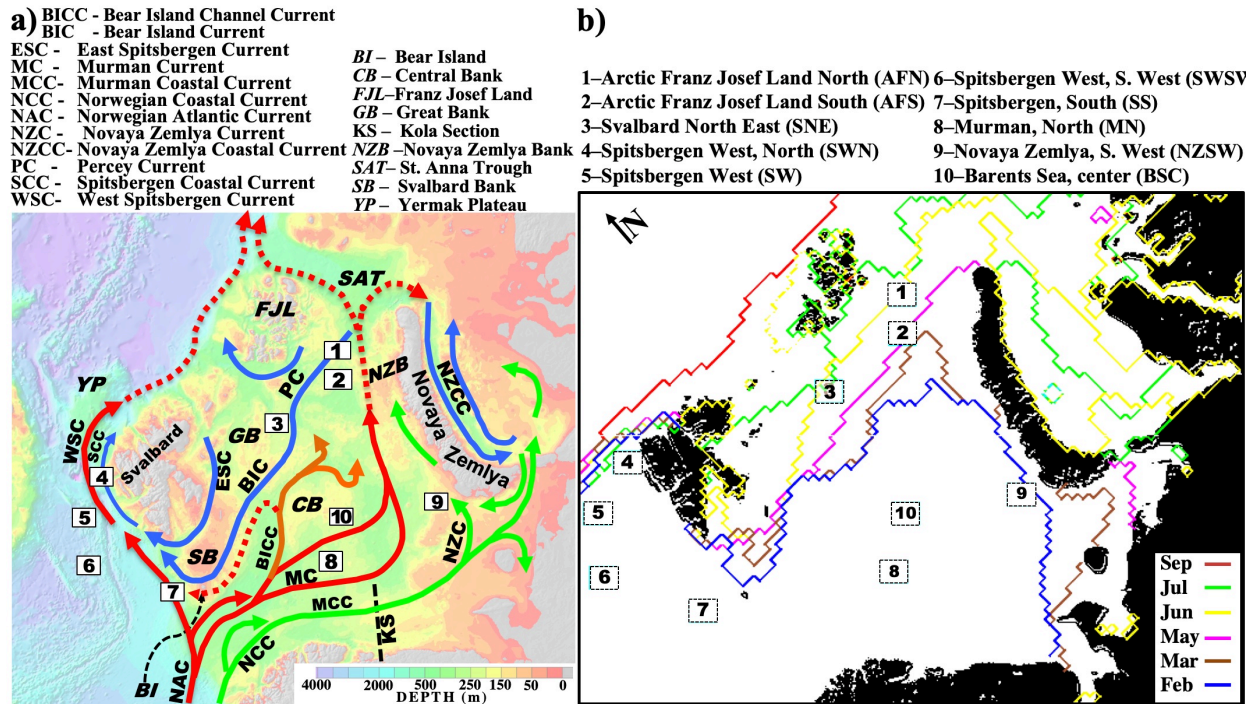


Figure 4. a) Simplified currents for Barents and nearby seas, bathymetry features, and focus-area boxes. Green, red, and blue arrows are coastal, warm Atlantic origin, and cold polar currents, respectively. Broken lines illustrate current subduction. Bathymetry from *M Jakobsson et al.* [2012]. **b)** Monthly ice extent for 2015. Focus study boxes (numbered); see **Supp. Table S1** for coordinates. Arrow points to North Pole. Barents Sea currents adapted from *J E Stiansen et al.* [2006]; for near Svalbard from *H Loeng* [1991]; see **Supp. Fig. S2** for greater detail for Svalbard area; for Kara Sea area from *L Polyak et al.* [2002]; see **Supp. Fig. S1** for greater detail. For Barents Sea Opening area from *R Bøe et al.* [2015]. East Barents Sea Currents from *V K Ozhigin et al.* [2011].

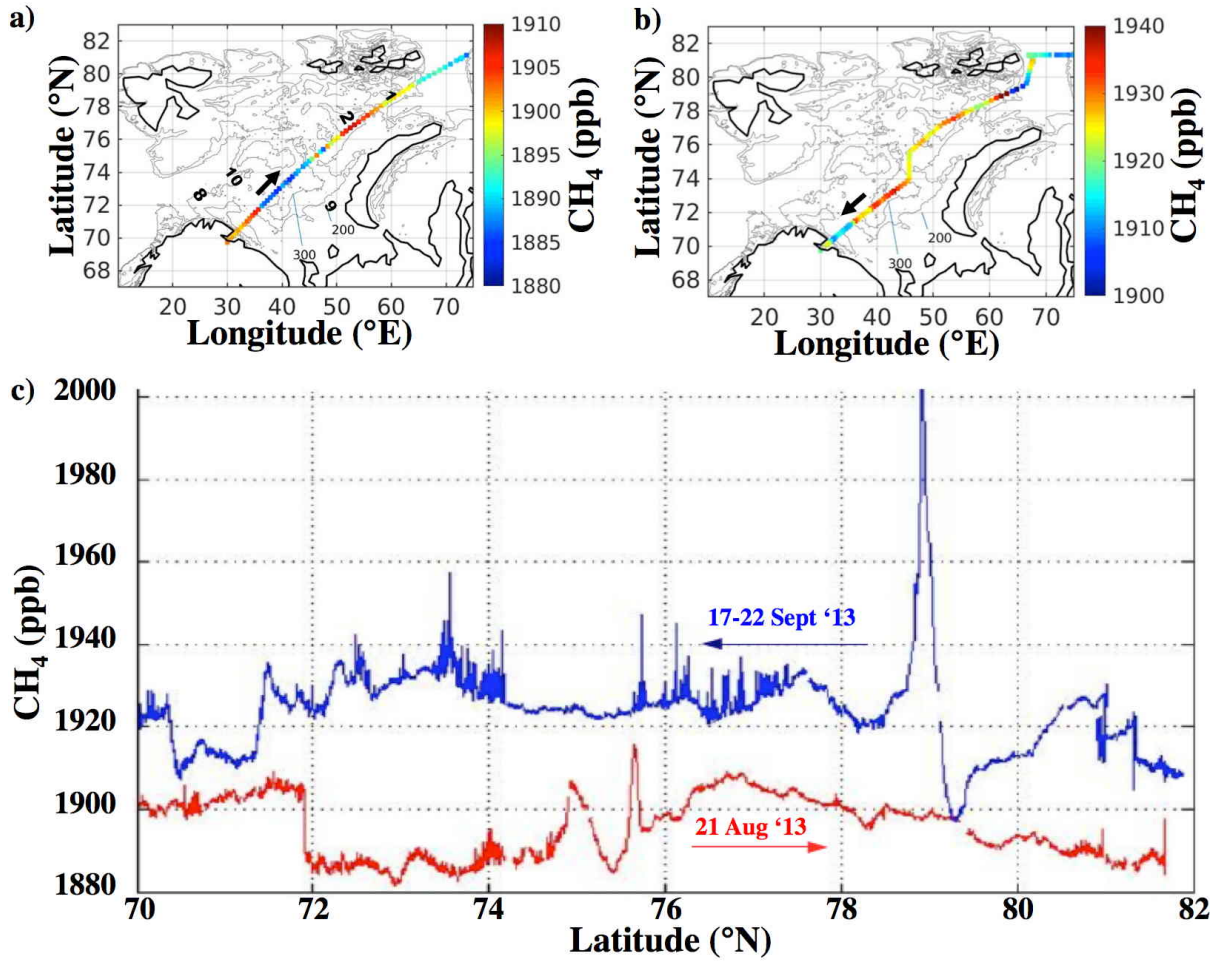


Figure 5. Surface *in situ* methane (CH₄) on the *R/V Akademik Fyodorov* for Barents Sea **a)** northwards transect for 21 Aug. 2013. Focus areas along pathway shown. **b)** Southwards transect for 17-22 Sept. 2013. Also shown is the 300-m depth contour and edges of the Murman Coastal Current, from PINRO (http://www.pinro.ru/labs/hid/kolsec1_e.htm). Note, Data key on figure. **c)** CH₄ profiles during northerly and southerly transits, labeled.

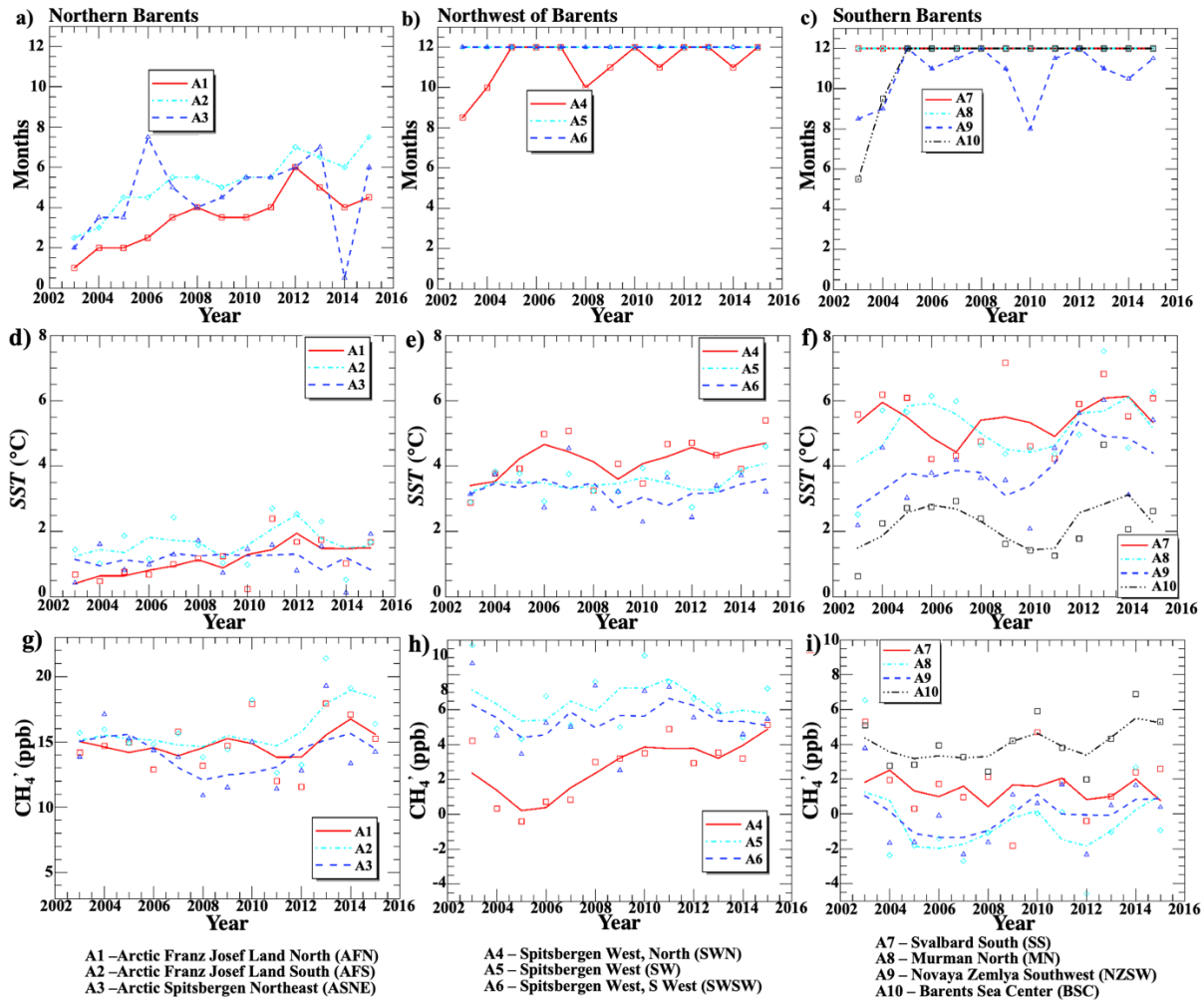
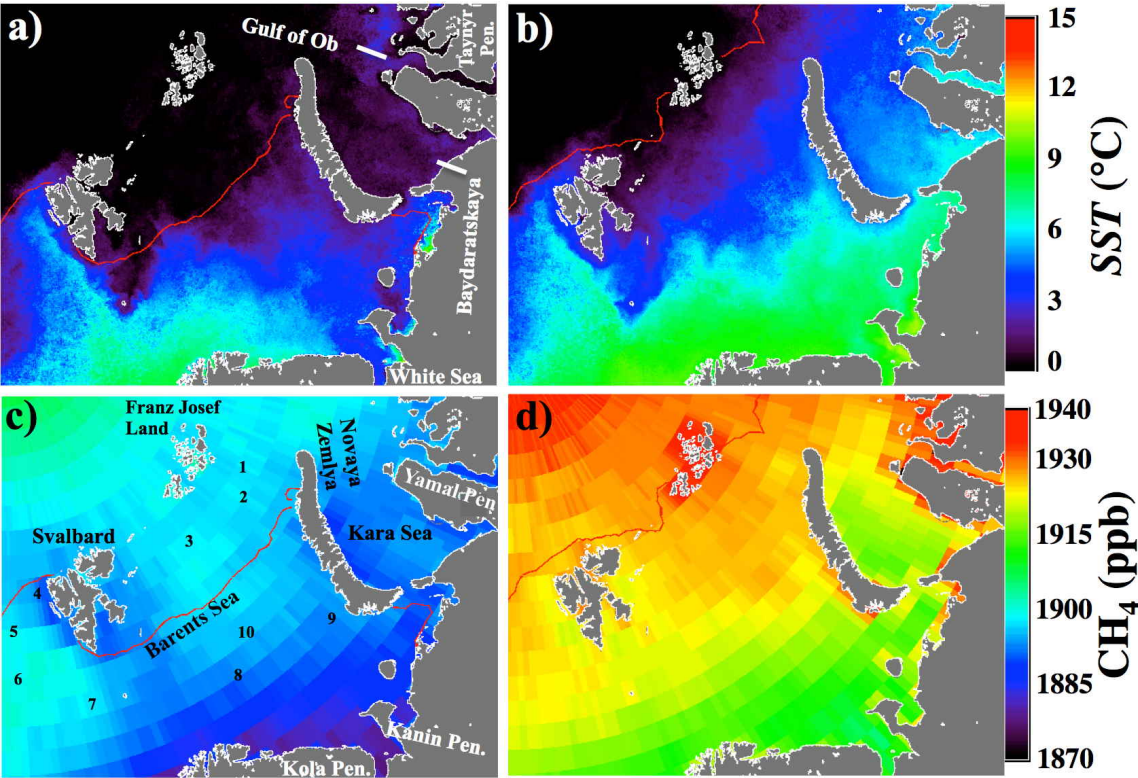


Figure 6. Focus study area time series for 2003-2015 for **a-c)** Ice-free months, labeled on figure, **d-f)** sea surface temperature (SST). Annual values are average of all months, generally May-October, which are ice-free, **g-i)** methane (CH₄). Annual data and 3 year, rolling-average data shown. Anomaly is relative to entire Barents Sea. Data key and focus area names on figure. See **Fig. 4a** and **Supp. Table S1** for locations.



925

926 **Figure 7.** Mean values for 2003 to 2015 of sea surface temperature (SST) for **a)** June and **b)** Sep-
927 tember. Mean methane (CH₄) concentration for **c)** June and **d)** September. Median ice edge for
928 same period is shown. Years with reduced ice extent contribute to values of SST north of this ice
929 edge. Data key on figure. See **Supp. Fig. S3** for overlay of currents.
930

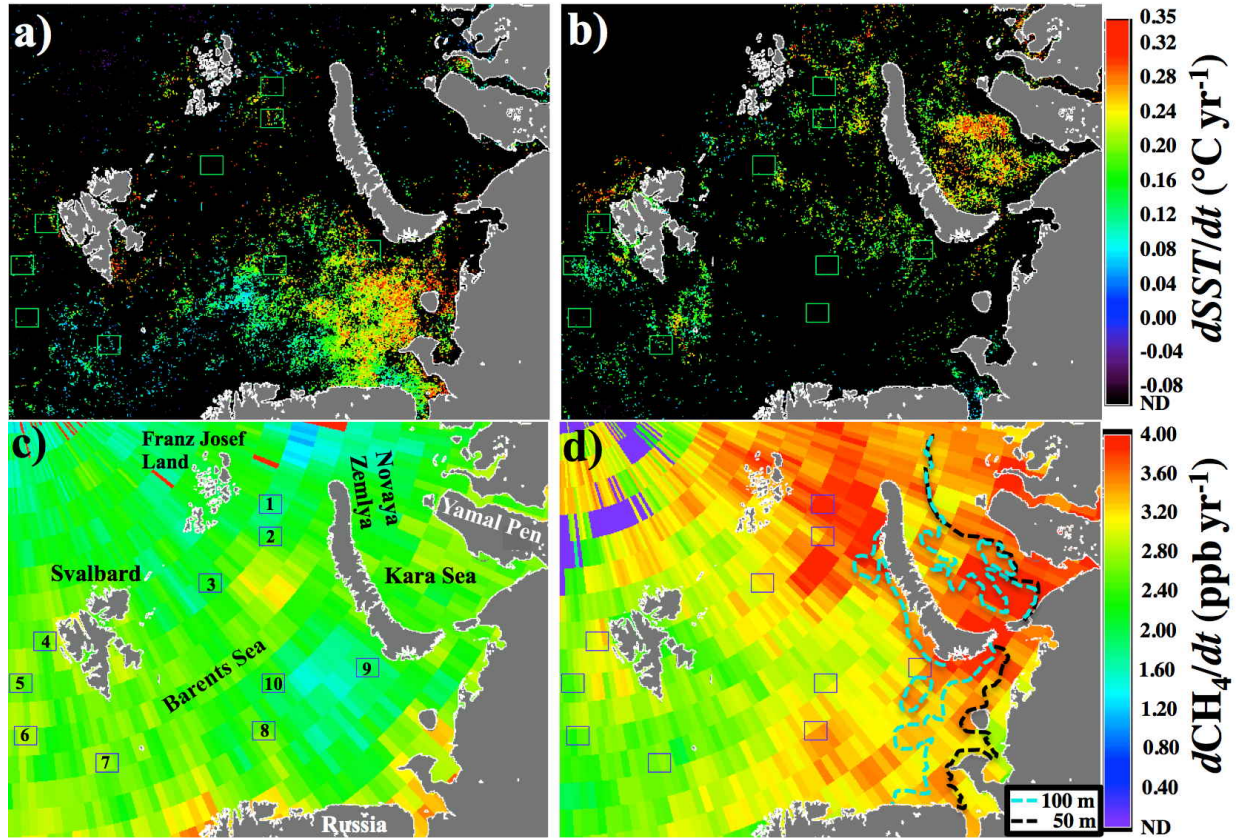


Figure 8. Linear trends for 2003 to 2015 of sea surface temperature ($dSST/dt$) for **a)** June and **b)** September. Methane concentration trend (dCH_4/dt) for **c)** June and **d)** September. ND – not detectable – failed statistical test. Blue, black dashed lines show 100 and 50 m contour, respectively. Data key on figure.

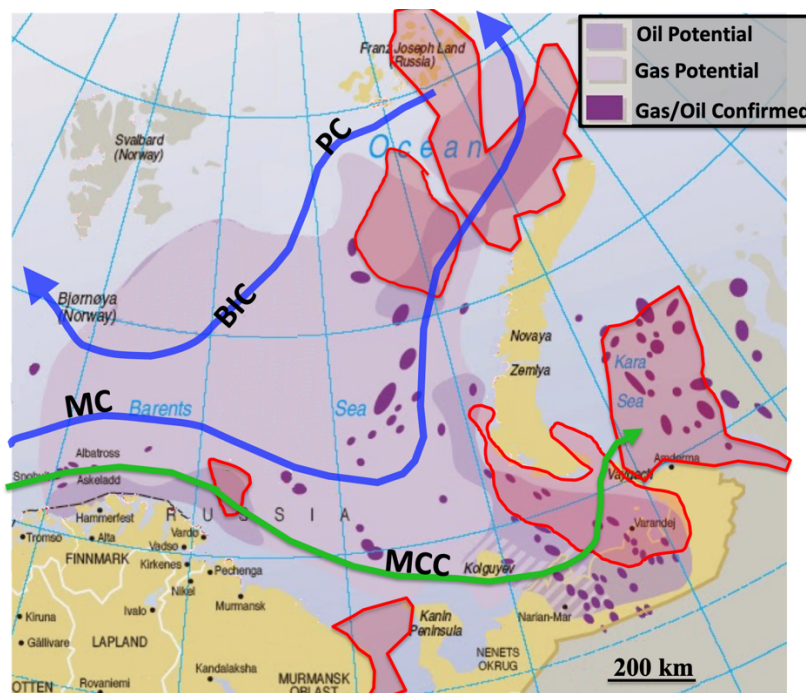


Figure 9. Barents Sea location of oil and gas fields and potential fields, and pipelines. Also shown are the approximate locations of the major Barents Sea currents – the Murman Current (MC), Murman Coastal Current (MCC), Bear Island Current (BIC), and Percey Current (PC). Areas outlined in red are where $dCH_4/dt > 3 \text{ ppb yr}^{-1}$ from **Fig. 6i**. Adapted from *P. Rekacewicz* [2005].

**Satellite ice extent, sea surface temperature, and atmospheric methane
trends in the Barents and Kara Seas**

**Ira Leifer¹, F. Robert Chen², Thomas McClimans³, Frank Muller Karger², Leonid
Yurganov⁴**

¹ Bubbleology Research International, Inc., Solvang, CA, USA

² University of Southern Florida, USA

³ SINTEF Ocean, Trondheim, Norway

⁴ University of Maryland, Baltimore, USA

Correspondence to: Ira Leifer (ira.leifer@bubbleology.com)

Supplementary Material

S1. Review of Airborne Arctic Methane measurements

CH₄ concentration profiles over the Arctic Ocean were measured on five flights during the HIAPER Pole-to-Pole Observations (HIPPO) campaign [E A Kort *et al.*, 2012; S C Wofsy, 2011] and produced evidence of sea surface CH₄ emissions from the northern Chukchi and Beaufort Seas in most profiles, up to 82°N. Enhanced concentrations near the sea surface were common over fractured floating ice in sample profiles collected on 2 Nov. 2009, 21 Nov. 2009, and 15 Apr. 2010. On 13 Jan. 2009 and 26 Mar. 2010, when the seasonally highest level of sea-ice coverage occurred, CH₄ emissions were weak or non-existent. Some of the observational variability was correlated with carbon monoxide (CO), indicating terrestrial origin.

The Carbon in Arctic Reservoirs Vulnerability Experiment (CARVE) program sought to quantify Alaskan CO₂ and CH₄ fluxes between the atmosphere and surface terrestrial ecosystems. Intensive aircraft campaigns with ground-based observations were conducted during summer from 2012-2015 [R Y-W Chang *et al.*, 2014]. No open ocean measurements were made. Additional Alaskan airborne data were collected summer 2015 (Jun.-Sept.) by the Atmospheric Radiation Measurements V on the North Slope of Alaska (ARM-ACME) project (38 flights, 140 science flight hours), with vertical profile spirals from 150 m to 3 km over Prudhoe Bay, Oliktok Point, Barrow, Atkasuk, Iqotuk, and Toolik Lake. Continuous data on CO₂, CH₄, CO, and nitrous oxide, N₂O, were collected [S C Biraud, 2016].

West of Svalbard, an area of known widespread seabed CH₄ seepage aligned along a north-south fault parallel to the coast [S Mau *et al.*, 2017; G K Westbrook *et al.*, 2008] was the focus of a field airborne campaign June–July 2014 [C L Myhre *et al.*, 2016]. Flights were conducted using the Facility for Airborne Atmospheric Measurements (FAAM) of the Natural Environment Research Council (NERC, UK). The campaign measured a suite of atmospheric trace gases and was coordinated with oceanographic observations. Seabed CH₄ seepage led to significantly increased seawater CH₄ concentrations. However, no significant atmospheric CH₄ enhancement was observed for the region above the seeps for summer data collected 20 Jun.–1 Aug. 2014 [C L Myhre *et al.*, 2016] under mostly light winds.

S2. Satellite Arctic AIRS and IASI Methane Measurement and Validation

A number of current orbital TIR instruments observe CH₄ [D J Jacob *et al.*, 2016] including the Tropospheric Emission Spectrometer (TES) [J Worden *et al.*, 2012], the Cross-Track Infrared Sounder (CrIS) [A Gambacorta, 2013], InfraRed Atmospheric Sounder Interferometer (IASI) [C Clerbaux *et al.*, 2009], and the Atmospheric Infrared Sounder (AIRS) [Hartmut H. Aumann *et al.*, 2003].

IASI CH₄ validation has been addressed in a number of studies for the lower and mid-upper Arctic troposphere. The EuMetSat IASI instruments are cross-track-scanning Michelson interferometers onboard the MetOp-A and MetOp-B platforms [C Clerbaux *et al.*, 2009]. IASI-1 (2007-) and IASI-2 (2013-) follow sun synchronous orbits. Three IASI New Generation instruments [C Crevoisier *et al.*, 2014] are planned for launch in 2021, 2028, and 2035 [IASI-NG, 2017].

IASI instruments measure in 8461 channels at 0.5 cm⁻¹ spectral resolution from three spectrometers spanning 645 to 2760 cm⁻¹. These spectrometers have a 2×2 array of circular footprints with a nadir spatial resolution of 12 km that is 39×25 km at swath (2400 km) maximum [C Clerbaux *et al.*, 2009]. IASI-1 was launched into an 817 km-altitude polar orbit on 19 Oct. 2006, while IASI-2 was launched on 17 Sept. 2012. MetOp-A and MetOp-B cross the equator at approximately 09:30 and 21:30 local time, separated by approximately half an orbit, resulting in twice daily, near-global coverage with 29-day revisit. The on-flight noise-equivalent delta temperature at 280K is estimated to be well below 0.1K in the spectral range of interest to CH₄ [A Razavi *et al.*, 2009]. IASI has a wide swath with a scan angle of ±48.3°. IASI CH₄ retrieval algorithms are described by X Xiong *et al.* [2013] and A Gambacorta [2013].

In the TIR, the AIRS (Atmospheric InfraRed Sounder) mission onboard the Earth Observation Satellite, Aqua satellite [Hartmut H. Aumann *et al.*, 2003] and the EuMetSat IASI-1 mission, on the MetOp-A platform [C Crevoisier *et al.*, 2014] [C Clerbaux *et al.*, 2009] provide long-term arctic CH₄ observations with new IASI instruments planned for launch in 2021, 2028, and 2035 [IASI-NG, 2017].

AIRS is a grating diffraction nadir cross-track scanning spectrometer on the Aqua satellite (2002-) that is part of the Earth Observation System [H.H. Aumann *et al.*, 2003]. AIRS was launched into a 705-km-altitude polar orbit on the EOS Aqua spacecraft on 4 May 2002. The satellite crosses the equator at approximately 01:30 and 13:30 local time, producing near global coverage twice a day, with a scan angle of $\pm 48.3^\circ$. Effective field of view after cloud clearing, is 45 km [J Susskind *et al.*, 2006] and the CH₄ spectral resolution is 1.5 cm⁻¹ from the 7.8 μ m TIR channel [Hartmut H. Aumann *et al.*, 2003]. Version 6 of AIRS Levels 2 and 3 data are publicly available [AIRS, 2016]; see X Xiong *et al.* [2010] for a description, evaluation, and validation of global CH₄ AIRS retrievals. Lower-troposphere (0-4 km altitude averaged) AIRS profiles are analyzed herein because the AIRS time series is longer than IASI.

AIRS CH₄ validation has been addressed in X Xiong *et al.* [2010], who compared aircraft data taken over Poker Flat, Alaska, and Surgut, Siberia with AIRS CH₄ retrieved profiles. Agreement was within 1.2% with mean measured CH₄ concentration between 300–500 hPa; correlation coefficients were ~ 0.6 – 0.7 .

IASI validation [X Xiong *et al.*, 2013] over a large area was achieved during a quasi pole-to-pole flight of the National Science Foundation's Gulfstream V aircraft [S C Wofsy, 2011]. A bias of nearly -1.74% was found for 374–477 hPa and -0.69% for 596–753 hPa. L Yurganov *et al.* [2016] compared 5-year long IASI data for 0-4 km layer over a sea area adjacent to the Zeppelin Observatory, Svalbard, Norway, at 474 m altitude, operated by the Norwegian Institute for Air Research (NILU). Monthly mean values and monthly trends were in good agreement, but daily excursions did not correlate. L Yurganov *et al.* [2016] explained the latter by the observatory's location being near the top of the planetary boundary layer.

S3. Currents

S3.1. Barents and Kara Sea Currents

The Barents Sea is bounded to the south by northern Europe and to the north by two archipelagos, Svalbard and Franz Josef Land (FJL). To the east lies the large north-south oriented, Novaya Zemlya archipelago, beyond which is the Kara Sea; to the west lies the Norwegian Sea. In winter the Barents Sea is partially ice-covered, while it is almost ice-free in the summer

The North Atlantic is a significant source of Arctic Basin water, whose density increases by cooling. Some of this water flows into the Barents Sea, ~ 2 Sv (1 Sv = 10^6 m³ s⁻¹), varying seasonally [H Loeng *et al.*, 1997] with most returning to the North Atlantic as part of the global thermohaline circulation [K Aagaard and E C Carmack, 1989; E Carmack and F McLaughlin, 2011; M Yamamoto-Kawai *et al.*, 2008]. T A McClimans and J H Nilsen [1993] used a laboratory physical model simulation to duplicate most of the observed regional Barents Sea oceanographic features forced by the densities and volume fluxes of water from the Atlantic (the Norwegian Atlantic Current - NAC and the Norwegian Coastal Current - NCC) and Arctic Basin (Persey Current - PC) and Barents Sea hydrography. Key features produced were the general structure of fronts and major currents, etc., which were obtained without regional atmospheric forcing. This highlights the dominant importance of oceanography rather than meteorology to these features.

North Atlantic water flows through the Norwegian Sea, forming the NAC, one track of which becomes the West Spitsbergen Current (WSC), with the remainder flowing into the Barents Sea through the Barents Sea Opening as the North Cape Current [J Piechura and W Walczowski, 2009]. The North Cape Current bifurcates into several forks mostly flowing to the east along the southern slope of the Barents Sea becoming the Murman Current (MC) near Murman.

The NAC is the major contributor of oceanic heat to the Barents Sea [V S Lien *et al.*, 2017]. Regional winds modulate the volume flow of Atlantic water into the Barents Sea—stronger in winter and weaker in summer [J E Stiansen *et al.*, 2009; Fig. 2.3.4]. Ice processes further complicate heat re-distribution for surface Arctic Ocean waters – ice insulates the water (better preserving the water’s heat) from atmospheric radiative cooling. For example, the NAC’s western fork (the WSC) submerges north of Spitsbergen (location varying seasonally) under an isolating layer of colder and fresher water furthering heat transport into the Arctic [V S Lien *et al.*, 2013; V S Lien *et al.*, 2017].

A south fork of the NAC is entrained into the NCC, which is 90% Atlantic water and 10% river discharge [Ø Skagseth *et al.*, 2008]. The NCC is a major contributor of oceanic heat to much of the southern and eastern Barents Sea and into the Kara Sea [V S Lien *et al.*, 2013]. The NCC cools significantly through interaction with the atmosphere. Upon entering Russian waters, the NCC is renamed the Murman Coastal Current (MCC). Long-term (1905-) temperature data for the upper 200 m are available from a section off the Kola Peninsula (**Fig. 4a, Kola Section, black dashed line**), which the MCC crosses [V D Boitsov *et al.*, 2012]. These data reveal long-term trends with a cooler period from 1875-1930 and continuous warming of ~0.8°C since a minimum in 1970-1980 [Ø Skagseth *et al.*, 2008]. The Kola Section data (which is full water column) show good gross agreement with long-term (since 1850) Barents Sea ice-extent [J E Walsh *et al.*, 2016] – the warm period from 1930-1965 corresponds to a significant reduction of spring sea-ice (from ~0.2 to ~0.12). The Kola Section data shows steady warming since 1970 that corresponds to a consistent general sea-ice extent decrease since 1980 in spring and since 1970 in fall. This highlights that important long timescale forcing by the MC and MCC affects sea ice extent, meteorology, and oceanography in the southern and eastern Barents Sea.

Although beyond this study’s scope, changes in the NAC/MC flow through the Kola Section relate to larger oceanographic trends. Ø Skagseth *et al.* [2008] found good agreement in the Kola Section temperature trend with the Atlantic Multi-decadal Oscillation (AMO) index. SST lags atmospheric temperatures by 2-3 months, peaking for the Kola area (offshore Murman, Russia) between 0 and 200 m in September-October, whereas air temperature peaks in July [J E Stiansen *et al.*, 2009, Figs. 2.3.3, 2.3.8].

The MCC continues eastward along the northern edge of the White Sea, becoming the Novaya Zemlya Current (NZC) until diverted northwards by Novaya Zemlya. It continues into the Arctic Basin through the Saint Anna Trough (SAT) between Franz Josef Land and Novaya Zemlya [H Loeng, 1991], which is the dominant outflow of the Barents Sea [W Maslowski *et al.*, 2004]. A fork of the MCC flows eastward into the Kara Sea through the narrow and shallow (20-50 m) Kara Strait (**Supp. Fig. S1** shows detailed Kara Sea currents).

A fork of the North Cape Current flows north through the Bear Island Channel towards the Hopen Deep (Loeng *et al.*, 1997), underneath the cold, south-flowing Bear Island Current (BIC). J A Whitehead and J Salzig [2001] suggested (and demonstrated in the laboratory) that remote forcing of the NAC through the Barents Sea lifts the current by several hundred meters to the sill of the Bear Island Channel, forcing significant anticyclonic vorticity. This drives the retrograde Bear Island Channel Current (BICC, our connotation) northeast along the slope of Svalbard Bank and the prograde Murman Current (MC) along the slope of Tromsøflaket, eastward and north to the east of the Central and Great Banks [S Li and T A McClimans, 1998; H Loeng, 1991]. S Li and T A McClimans [1998] referred to the BICC as the “Warm Core Jet” to emphasize its physical significance at the Polar Front. These merge east of the Central and Great Banks. The resulting flow cools from contact with the atmosphere into a denser, modified Atlantic Water flow that exits through the Saint Anna Trough to the east of Franz Joseph Land [T Gammelsrød *et al.*, 2009]. Cooling at these banks also produces a dense westward underflow, depicted by the dashed line in **Fig. 4a**.

The Percey Current transports cold, low saline, Arctic surface water into the Barents Sea to the east of Spitsbergen, becoming the Bear Island Current (BIC) to the west of the Grand Bank (**Supp. Fig. S2**). The Percey Current meets warmer, higher salinity waters of Atlantic origin in the Barents Sea, giving rise to the Barents Sea Polar Front [L Oziel *et al.*, 2016], whose location is controlled by seabed bathymetry, i.e., it is semi-stationary [G Gawarkiewicz and A J Plueddemann, 1995]. This front is part of a unique frontal system due to its combination with the seasonally ice-covered zones in the northern, central, and eastern Barents Sea [T Vinje and Å S Kvambekk, 1991]. Part of the Percey Current merges with the East Spitsbergen Current (ESC) to the west of the Svalbard Bank and then flows north along

the west Spitsbergen coast, inshore of the WSC, as the Spitsbergen Coastal Current (SCC). This flow loops the Barents Sea Polar Front around Spitsbergen [H Svendsen *et al.*, 2002].

S3.2. Detailed Kara Sea Currents and Bathymetry

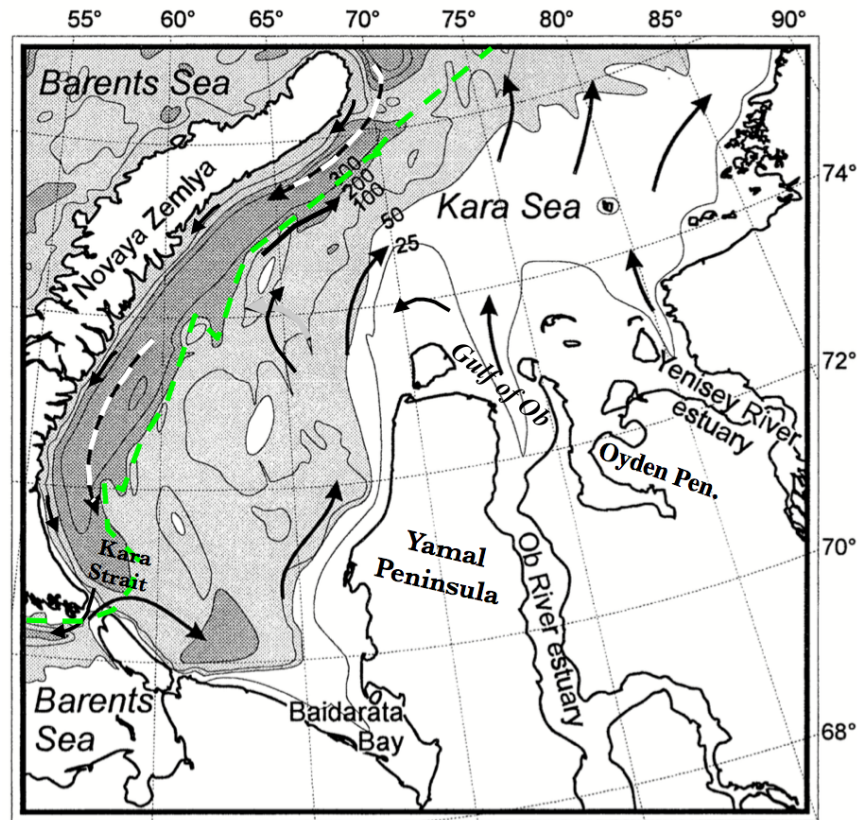


Figure S1. Bathymetry and currents for the Kara Sea. Adapted from *L Polyak et al.* [2002] and *T A McClimans et al.* [2000]. Dashed line indicates subsurface flows. Green line shows approximate edge of submerged permafrost from *T E Osterkamp* [2010].

Kara Sea hydrography is controlled by the freshwater outflow of the Ob and Yenisei Rivers (**Fig. 2b; Supp. Fig. S1 for finer details**), which contribute 350 and 650 km³ yr⁻¹, respectively [C A Stedmon *et al.*, 2011], approximately double that of the Mississippi River, primarily (>75%) between May and September. As a result, the eastern Kara Sea is brackish. Riverine sediment leads to the northeast Kara Sea being mostly shallow (< 50 m). The western Kara Sea is deep (mostly >100 m), descending to below 500 m in the Novaya Zemlya Trough [L Polyak *et al.*, 2002].

Cold Arctic waters, and ice and melt water from Novaya Zemlya flow southward along the eastern shore of the Novaya Zemlya Archipelago in the narrow, weak Novaya Zemlya Coastal Current (NZCC). Inflow of modified Atlantic water from the Barents Sea (dashed line in **Fig. S1**) accounts for a warm core in the deep Novaya Zemlya Trough [see T A McClimans *et al.*, 2000, Section 11]. Part of the NZCC exits through the same Kara Strait that Barents Sea coastal water enters. This, in combination with the rising shallow seabed, causes the Kara Strait to be a site of strong mixing.

Deeper water in the trough is supplied by inflow of modified Atlantic water from the northern Barents Sea. On the surface, inflows to the north Kara Sea come from the MCC, local runoff, and ice in the Novaya Zemlya Coastal Current (NZCC), with some flow returning to the Barents Sea through the Kara Strait. Warmer water enters the south Kara Sea from the Barents Sea as the MCC flows through the Kara Strait, joining a northward flowing slope current.

Much of this water mixes with the southern flowing NZCC and returns to the Barents Sea through the Kara Strait [T A McClimans *et al.*, 1999; T A McClimans *et al.*, 2000].

The Ob and Yenisei Rivers transport significant sediment, underlying the shallowness of the Kara Sea, with extensive proven and proposed petroleum hydrocarbon reservoirs underlying the east and southeast Kara Sea [P Rekacewicz, 2005]. Given the Kara Sea's shallowness, CH₄ seep seabed bubbles can mostly transfer their gas directly to the atmosphere [I Leifer and R Patro, 2002; I Leifer *et al.*, 2017] and indirectly from wind mixing [R Wanninkhof and W R McGillis, 1999], and also from storm sparging [V D Boitsov *et al.*, 2012; N Shakhova *et al.*, 2013], which in the Arctic can extend to 100-200 m depth, i.e., most of the Kara Sea.

S3.3. Detailed West Barents Sea Currents and Bathymetry

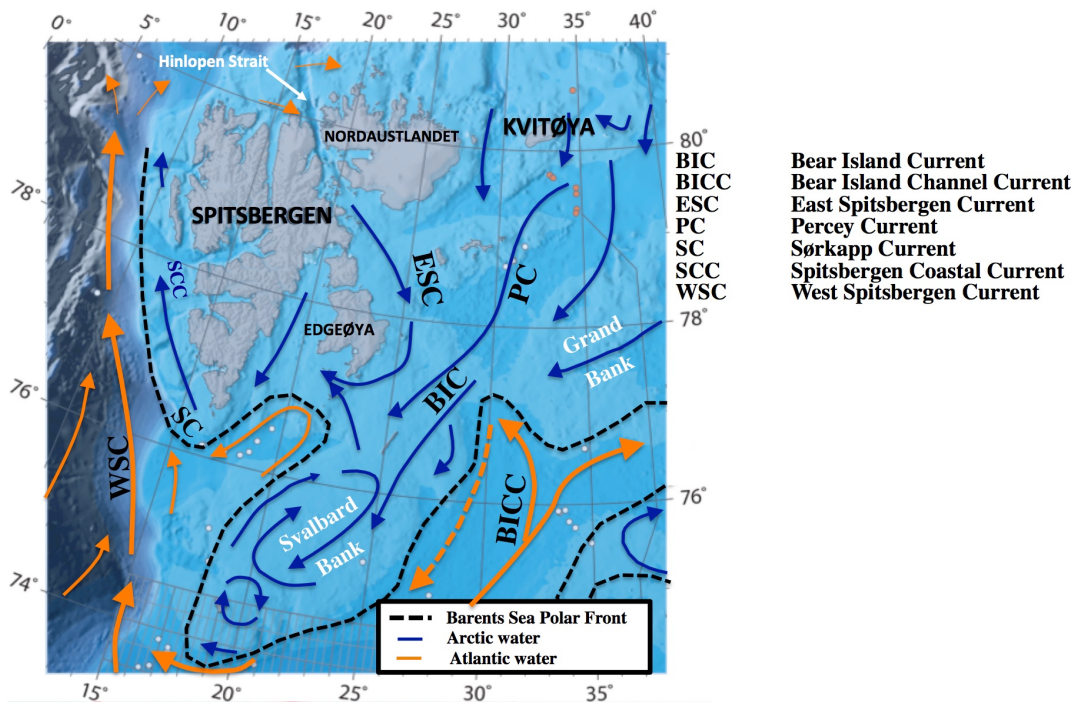


Figure S2. Bathymetry and currents around Svalbard. Bathymetry from Norwegian Petroleum Directorate [2016]. Currents from H Loeng [1991]. Dashed black line shows location of the Barents Sea Polar Front, Dashed currents are submerged; blue - cold, orange - warm.

Currents and flows around Svalbard Archipelago are complex (Fig. S2), dominated by the West Spitsbergen Current (WSC), which is the northerly fork of the Norwegian Atlantic Current (NAC), and flows northwards off the west coast of Spitsbergen. The cold, Percey Current (PC) flows southwest off the eastern shores of the Svalbard Archipelago. The cold East Spitsbergen Current (ESC) flows through the Hinlopen Strait and then joins the PC to flow around the south cape of Spitsbergen as the Sørkapp Current (SC), following the coast northwards as the Spitsbergen Coastal Current (SCC) [H Svendsen *et al.*, 2002]. The cold SCC flows inshore of the WSC, and flows up Svalbard's western coast, inshore and shallower than the warm, Atlantic WSC. The interface between these two currents off west Spitsbergen forms a part of the Barents Sea Polar Front. Thus, coastal waters offshore West Spitsbergen are of Barents Sea / Atlantic water origin, whereas further offshore lies Barents Sea water (origin Atlantic Ocean).

The location of the Barents Sea Polar Front [L Oziel *et al.*, 2016] is semi-permanent and controlled by seabed topography (Fig. S2), particularly the Svalbard Bank, the Great Bank, and the trough south of Spitsbergen.

The energy budget of the Barents Sea is driven by Atlantic heat input by the two forks of the NAC (Fig. S3) [V S Lien *et al.*, 2013], strongly impacting the Barents Sea SST climatology (Fig. S3). Along one fork, warmer water flows

eastward along the northern Norwegian, Murman, and then western Novaya Zemlya coasts towards the north. The other NAC fork flows northeast along the Svalbard Bank (SB). These flows closely correspond to “tendrils” of warmer water extending north to the east of the Central Bank and to the west of Novaya Zemlya and around Bear Island (**Fig. S3a**) and in September in the east Barents Sea (**Fig. S3b**). In June, winds oppose this climatology, i.e., *SST* is most strongly influenced by ocean current transport. In fall, currents and winds are aligned along the Norwegian and Murman and western Novaya Zemlya coasts, reinforcing the transport of heat as indicated in *SST*. Note, though much of the heat that these winds transport originates from the NAC, which maintains Norway at temperatures well above latitudinal averaged. Still, winds cannot explain the spatial distribution of warm *SST*, which extends into the calm around the Central Bank.

Water becomes cooler as it penetrates eastward, and as it reaches the (seasonally varying) ice edge (**Fig. S3**). Across much of the Barents Sea there is a strong latitudinal *SST* gradient extending south from the ice edge, independent of the location of the eastern NAC branches. In the coastal waters off western Novaya Zemlya, where the warm NZC flows, water extends further north than elsewhere into areas where winds are from the north (**Fig. 4a**). Moreover, regions with statistically significant warming *SST* trends ($dSST/dt$) were in areas of northerly winds both in June and September.

[J C Comiso et al., 2008]

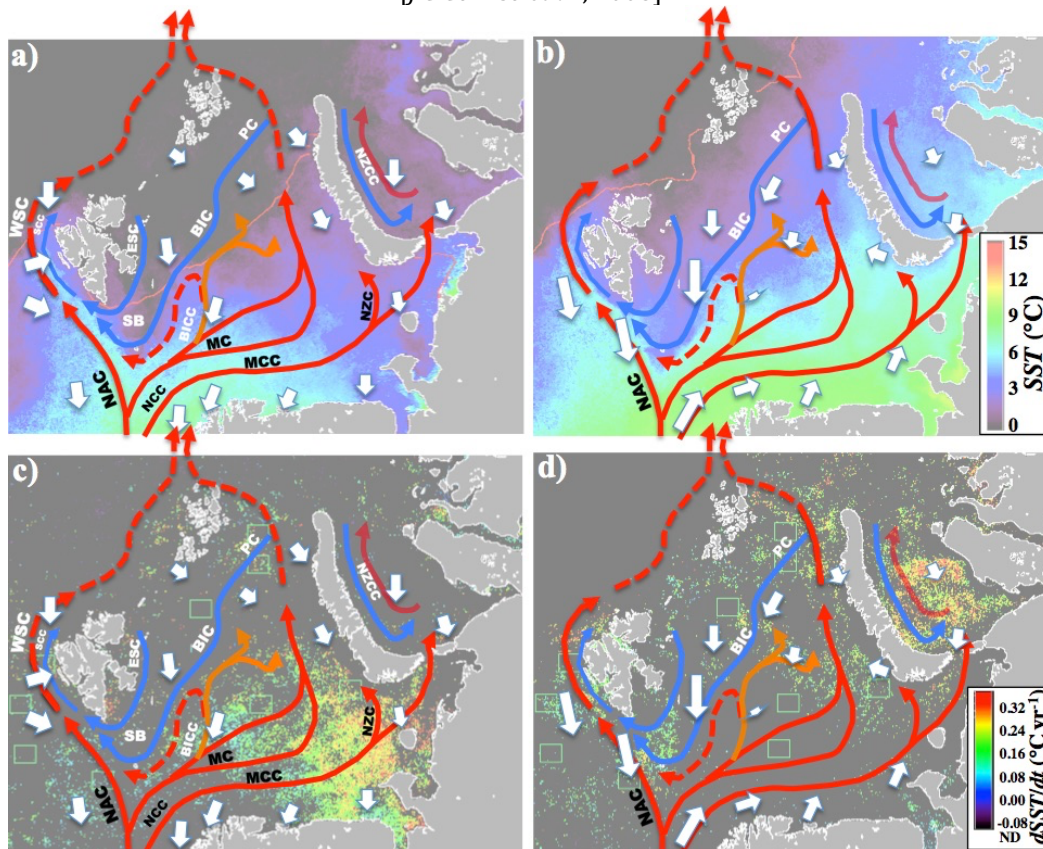


Figure S3. Warm and cold currents (from **Fig. 4a**) superimposed on **a)** June and **b)** September for climatology *SST*, and **c)** June and **d)** September for $dSST/dt$ trends (ND-no trend detected). The red line shows ice location. Red and blue arrows show warm and cold currents, respectively. Dashed line indicates subsurface flow. Winds (white arrows) are adapted from *E W Kolstad* [2008].

S4. Winds in the Barents and Kara Sea

Accessible meteorological data for the Barents Sea, outside of west Svalbard, whose meteorology and oceanography are affected by the Greenland Sea, are difficult to find, e.g., *V D Boitsov et al.* [2012] for Bear Island, except for sites

on the northern Norwegian and Murman coasts. In this regard, the Murmansk airport weather data are the most eastward available long-term data representing southern Barents Sea, coastal meteorology and oceanography. Daily average meteorology data for 2002-2018 were downloaded (<https://www.wunderground.com/weather/ru/murmansk>) and segregated by month, and found a warming of $0.12^{\circ}\text{C yr}^{-1}$ in June and $0.11^{\circ}\text{C yr}^{-1}$ in September. Over this period, winds strengthened slightly ($0.0173 \text{ m s}^{-1} \text{ yr}^{-1}$) with most of the increase in September occurring in 2017 and 2018 (**Fig. S4**). These warming rates are significantly faster than those at Bear Island, which reflects both the greater moderation of the marine rather than coastal atmosphere and the influence of the cold Bear Island Current. Winter temperatures increased even faster.

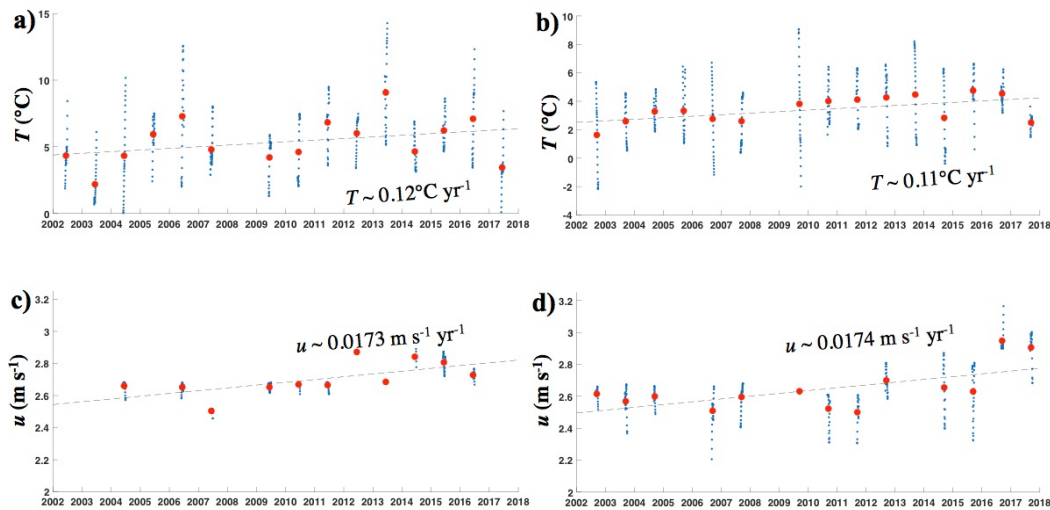


Figure S4. Wind and temperatures for Murmansk airport, Murman, Russia (68.7845°N , 32.7579°E) for **a)** June and **b)** September. Daily-averaged (blue) and monthly-averaged (red) data, and linear polynomial fits (red dashed line) are shown. Data from weatherunderground.com.

S5. Focus Areas

Table S1. Focused study area coordinates

Area	Upper Left	Upper Right	Lower Left	Lower Right
1	79° 16'6.91" N 60° 48'53.42" E	78° 32'12.26" N 62° 49'54.69" E	78° 55' 5.27" N 57° 43' 42.58" E	78° 12'27.81" N 59° 52'32.46" E
2	78° 38'25.09" N 55° 34'48.90" E	77° 56'45.71" N 57° 48'15.36" E	78° 14' 20.21" N 52° 49' 55.73" E	77° 34'0.24" N 55° 8'13.34" E
3	79° 10'4.24" N 41° 13'50.40" E	78° 36'13.19" N 44° 21'38.03" E	78° 38' 35.38" N 38° 57' 26.67" E	78° 6'12.61" N 42° 3'28.98" E
4	79°38'46.04" N 5° 40'51.21" E	79° 31'53.40" N 10° 11'25.49" E	78° 57' 49.65" N 5° 19' 46.85" E	78° 51'21.95" N 9° 34'7.45" E
5	78° 8'40.32" N 0° 36'30.89" E	78° 6'24.41" N 4° 35'53.20" E	77° 27' 29.19" N 0° 34' 31.46" E	77° 25'20.57" N 4° 20'54.29" E
6	76° 11'22.21" N 1° 16'10.96" E	76° 8'46.20" N 4° 41'44.27" E	75° 30' 6.27" N 1° 12'35.25" E	75° 27'37.48" N 4° 28'29.63" E
7	74° 48'24.40" N 12° 40'7.63" E	74° 36'9.07" N 15° 40'42.21" E	74° 8' 1.53" N 12° 7'35.64" E	73° 56'16.20" N 15° 1'6.10" E
8	73° 34'52.37" N 33° 48'43.77" E	73° 6'7.85" N 36° 8'55.31" E	73° 0'12.51" N 32° 31'37.62" E	72° 32'23.29" N 34° 49'20.56" E
9	72° 46'29.04" N 48° 59'20.20" E	72° 8'6.72" N 50° 44'6.03" E	72° 18'49.49" N 47° 18'49.40" E	71° 41'23.16" N 49° 4'27.27" E
10	74° 48' 6.77" N 38° 38'57.13" E	74° 16'3.18" N 41° 0'24.96" E	74° 15'28.49" N 37° 5'34.21" E	73° 44'27.53" N 39° 25'24.39" E

S6. Barents Sea *in situ* data

CO₂ and CH₄ *in situ* data were collected by a Cavity Enhanced Absorption Spectrometer (CEAS), Greenhouse Gas Analyzer (Los Gatos, Research, Mountainview, CA) onboard the *R/V Akademik Fyodorov* during the Nansen and Amundsen Basins Observational System (NABOS) expedition in fall 2013. The *R/V Akademik Fyodorov* is 141-m long with a 25-m beam and 8-m draught. The *R/V Akademik Fyodorov* departed Kirkenes, Norway on 21 Aug. 2013, returning to Kirkenes on 23 Sept. 2013. Analyzer performance information also was recorded for data quality review. Instrument precision was ~1 ppb with a 10 s response time and a 117 s mean layback time. Samples were collected from above the main superstructure, approximately 25 m above the sea surface (**Fig. S4a**), Calibration was daily and used a cylinder standard provided by the Norwegian Air Research Institute (NILU).

The main potential source of ship pollution could be the diesel engine exhaust; however, it appears that the *Akademik Fyodorov*'s engine is not a source of CH₄, with atmospheric CH₄ partially oxidized by the engine leading to exhaust gas having depressed CH₄ compared to ambient air. Data analyzed herein were during steaming transit across the Barents Sea at 26 km hr⁻¹, for which other potential vessel sources, such as the sewage storage venting are not relevant.

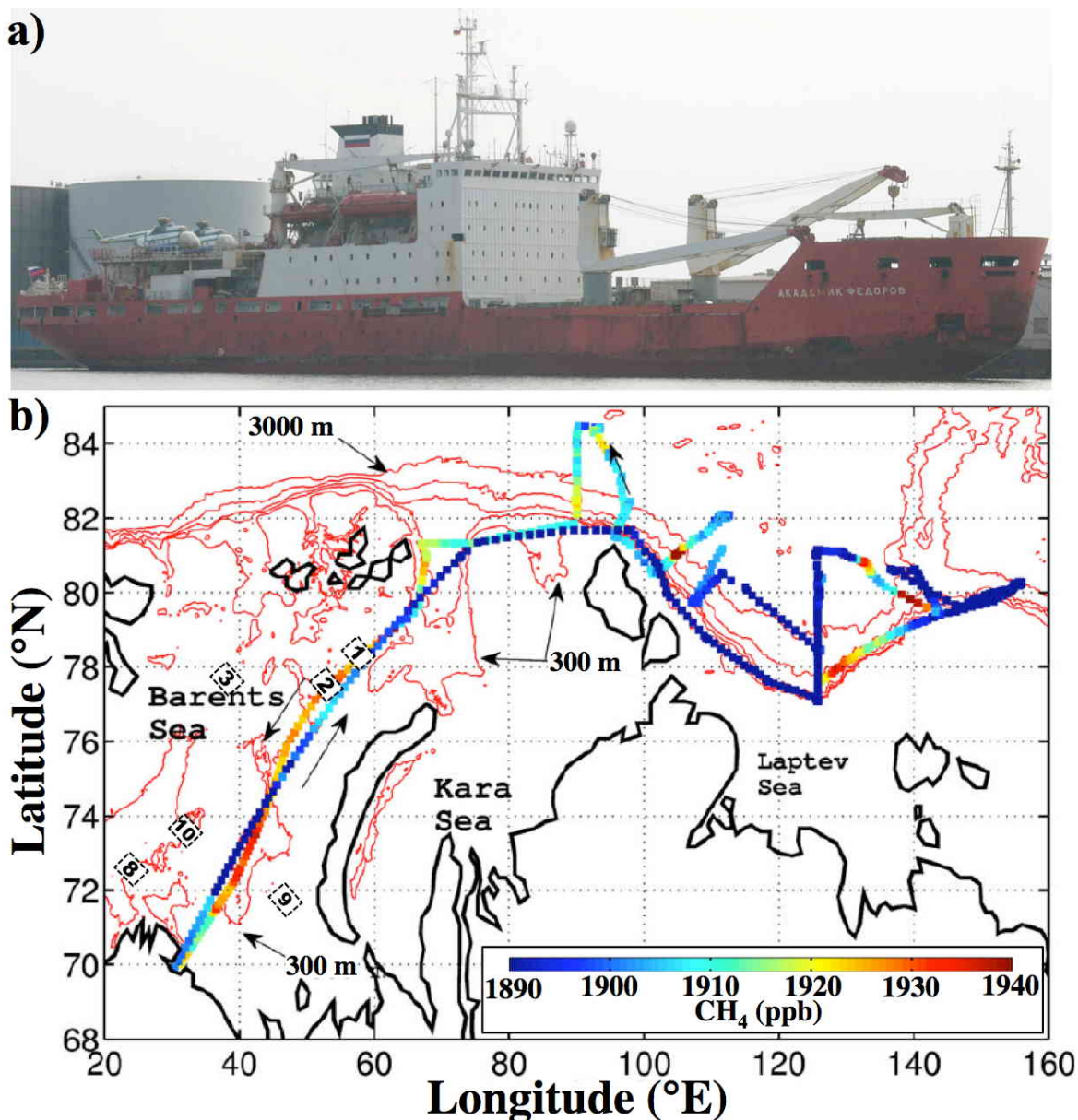


Figure S5. a) Photo of the *R/V Akademik Fyodorov*. **b)** Hourly averaged methane (CH_4) from NABOS expedition. Red shows 300 m depth of the hydrate stability field. Location of focus areas (**Table S1**) shown. Data key on figure.

The month-long data set showed a significant difference between the northwards and southwards transits of the Barents Sea, which were separated by approximately one month and passed directly through Focus areas 1 and 2, as well as between focus areas 9 and 10 in the southeast Barents Sea, approximately along the path of the Murman Current. Most of the CH_4 values in the Laptev Sea were low, although there were several locations of enhanced CH_4 . NABOS values were compared with satellite-retrieved column CH_4 from IASI for 21–24 Aug. 2013 for the northeastwards transit and for 17–22 Sept. 2013 for the southwestwards transit. Agreement between IASI lower tropospheric CH_4 and *in situ* CH_4 for the northwards transit was good, within ~ 10 ppb, whereas agreement was much poorer for the southwards transit.

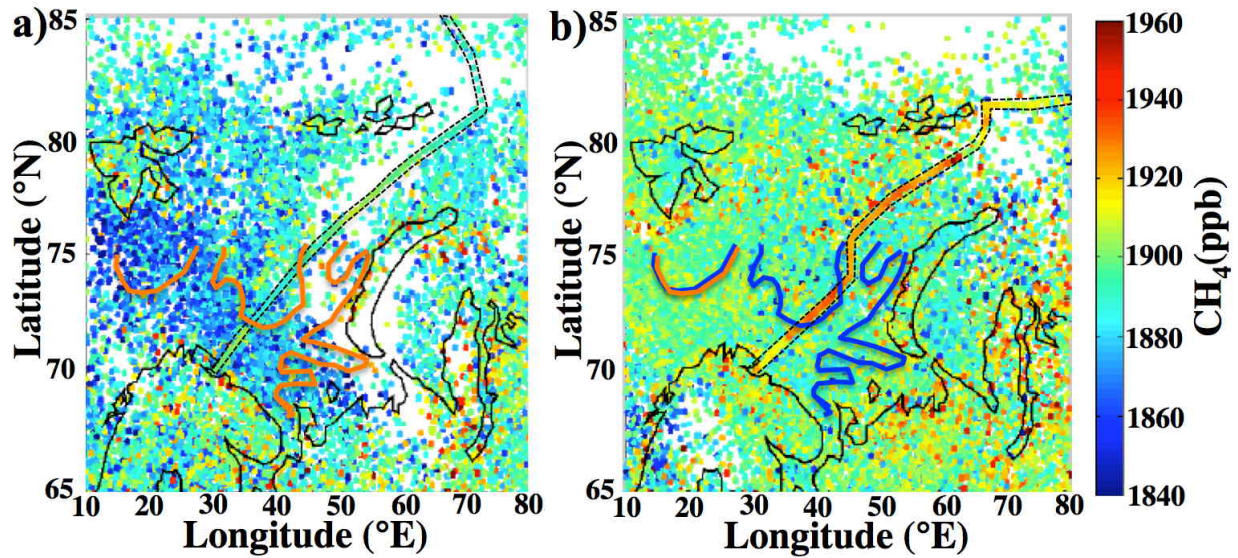


Figure S6. a) IASI retrieved 0-4 km methane (CH_4) for 21-24 Aug. 2013 and hourly CH_4 from the NABOS cruise (outlined in dashed line black). Also shown is the Murman Coastal Current's edges in orange and blue from *A P Alexeev et al. [2018]* and b) for 17-22 Sept. 2013. Data key on figure.

S7. Summer month sea surface temperature and methane trends

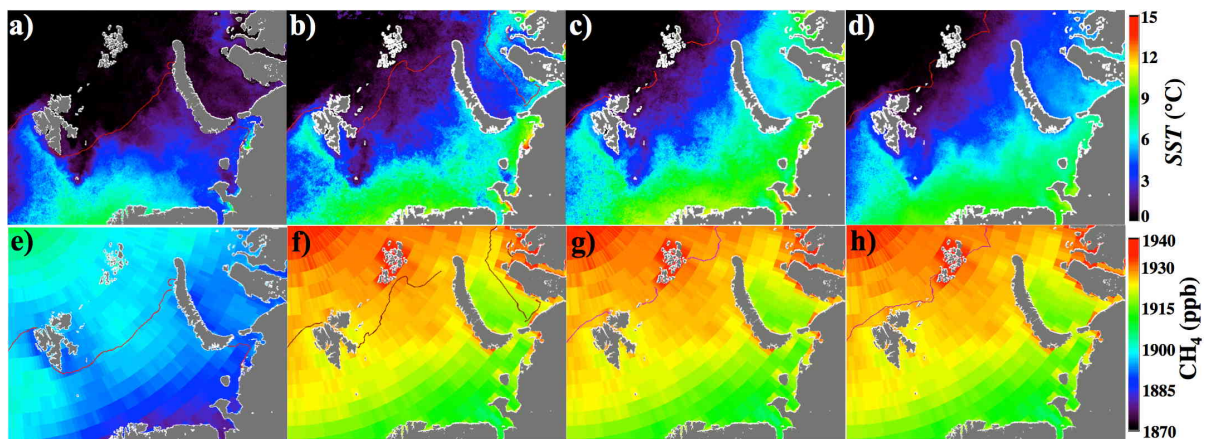


Figure S7. Mean values for 2003 to 2015 of sea surface temperature (SST) for a) June, b) July, c) August, and d) September. Mean methane (CH_4) concentration for e) June, f) July, g) August, and h) September. Median ice edge for same period is shown. Years with reduced ice extent contribute to values of SST north of the ice edge. Data keys on figure.

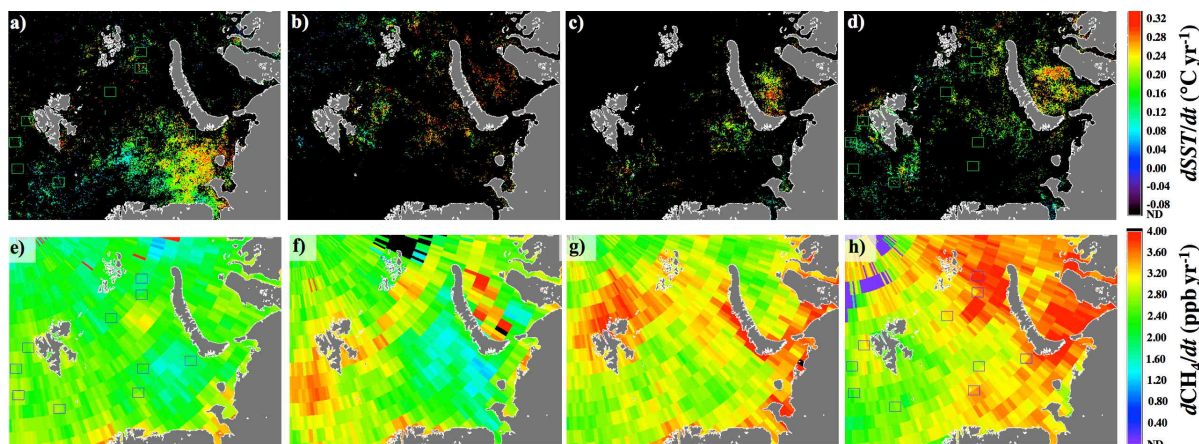


Figure S8. Linear trends for 2003 to 2015 of sea surface temperature ($dSST/dt$) for **a)** June, **b)** July, **c)** August, and **d)** September. Methane concentration trend (dCH_4/dt) for **e)** June, **f)** July, **g)** August, and **h)** September. ND – not detectable, i.e., failed statistical test. Blue, black dashed lines shows 100 and 50 m contour, respectively. Data key on figure.

S8. Implications for Svalbard area methane emissions

There are few atmospheric and ocean CH_4 data for the Barents Sea and surrounding areas, the most prominent being associated with CH_4 seepage off Spitsbergen, located immediately south of focus area A4. Studies to date have been in early summer; *S Mau et al.* [2017]; *C L Myhre et al.* [2016] sampled the atmosphere and water column while Westbrook et al. (2009) reported sonar observations of seep bubbles for August-September, and slightly elevated aqueous CH_4 in surface waters immediately above the bubble plumes. All concluded that transport to the atmosphere was not significant, attributed to trapping dissolved CH_4 below the pycnocline. It is important to note that with respect to the overall Barents Sea area CH_4 anomaly, the Svalbard area is far less important than waters around Franz Josef Land, off the west coast of Novaya Zemlya, and the north-central Barents Sea (**Fig. 9**).

Both SST and CH_4 in June (**Fig. 9**) and July (**Supp. Fig. S7**) show that much of the active seepage in west Spitsbergen show that much of the area of active seepage was inshore of the Barents Sea Polar Front, and thus under the cooling Arctic waters of the Spitsbergen Coastal Current (SCC), supported by reported salinity data (Mau et al., 2017). Although SST remains low off Spitsbergen in September, and extends further offshore, CH_4 concentrations no longer are depressed compared to Atlantic water further offshore, i.e., greater transport to the atmosphere. Such transport would not be expected downcurrent (north) of the bubble plumes observed by the early fall cruise reported in *G K Westbrook et al.* [2009].

Although the studies indicate these seeps do not contribute to summer atmospheric CH_4 , they did not consider methane shoaling, which would allow seabed CH_4 to reach the atmosphere far downstream. Interestingly, Mau et al. (2017; Fig. 3) show data that could be interpreted as methane shoaling with elevated aqueous CH_4 forced shallower by the north-flowing SCC, crossing subterranean ridges. Focus area A4 shows the strongest increase in CH_4 from 2005-and an increasing SST over this time period, consistent with shoaling. Stronger enhancement of CH_4 growth is observed north of Spitsbergen in June (**Fig. 10c**), which is the most likely location for shoaling based on detailed Svalbard bathymetry and currents (**Supp. Fig. S2**). Specifically, this is where some of the warm West Spitsbergen Current mixes with the cold, Spitsbergen Coastal Current (SCC) that would be CH_4 enriched from seabed seepage, and then flows over relatively shallow seabed towards the Hinlopen Strait. Thus, there is evidence of increasing downstream CH_4 transport to the atmosphere downcurrent of seepage off West Spitsbergen after methane shoaling, albeit not significant to overall Barents Sea emissions.

There is evidence of acceleration in the CH₄ growth nearshore off West Spitsbergen in June, but not in September (**Fig. 10d**) when CH₄ growth enhancement lies in the further offshore waters that are impacted by the warm WSC. Trends in *SST* also suggest a weakening of the Percey Current in June and more so in September. Given that from June to September the SCC extends further offshore, this suggests WSC control. Similarly, the WSC eastwards leg that crosses Nordaustlandet is driving a rapid increase in *SST* in September and likely relates to the increased CH₄ trend.

S9. Arctic Methane Movie

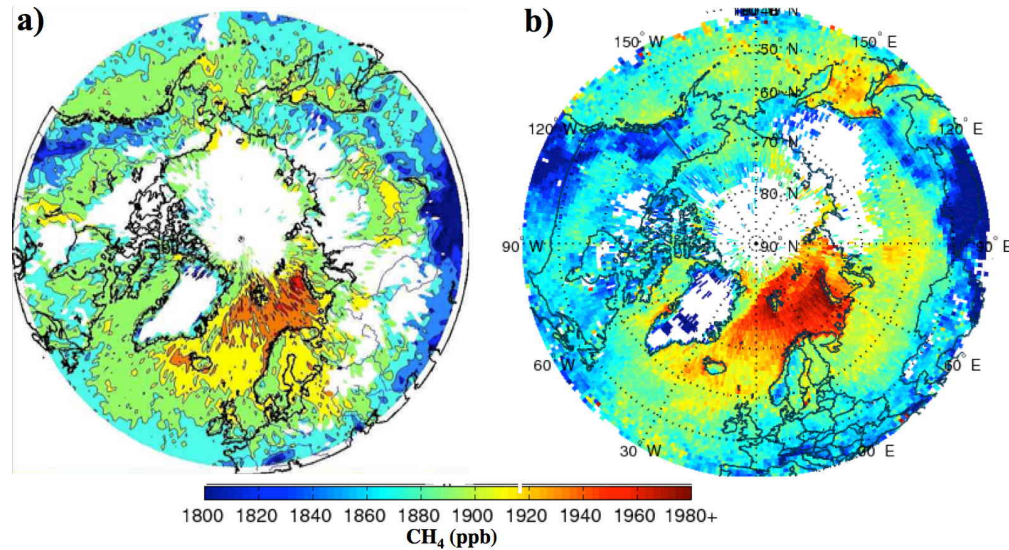


Figure S9. IASI Arctic methane (CH₄) for the lower 4 km for a) March 2012 and b) March 2018.

A movie of Arctic CH₄ from 2012 every 5 days shows a range of variations on a range of different spatial and temporal scales (**Fig. S9**). Strong enhancements are observed that persist in regions for a few days—most likely related to synoptic system flushing in fall to spring. The seasonal variation is easily observed, with highest values often in November and December. In late winter and early spring, large CH₄ anomalies are observed in some years at the ice edge.

Supplemental References

- Aagaard, K., and E. C. Carmack (1989), The role of sea ice and other fresh water in the Arctic circulation, *Journal of Geophysical Research: Oceans*, 94(C10), 14485-14498.
- AIRS (2016), Version 6 AIRS Level 2 and 3 CH₄ data, edited.
- Alexeev, A. P., A. V. Semenov, V. A. Borovkov, V. V. Tereshchenko, and V. N. Shleinik (2018), Historical review of oceanographic observations in the Kola section, edited, Polar Research Institute of Marine Fisheries and Oceanography (PINRO), Murmansk, Russia.
- Aumann, H. H., et al. (2003), AIRS/AMSU/HSB on the Aqua mission: design, science objectives, data products, and processing systems, *IEEE Transactions on Geoscience and Remote Sensing*, 41(2), 253-264.
- Aumann, H. H., et al. (2003), AIRS/AMSU/HSB on the Aqua mission: design, science objectives, data products, and processing systems, *IEEE Transactions on Geoscience and Remote Sensing*, 41(2), 253-264.
- Biraud, S. C. (2016), ARM-ACME V: ARM Airborne Carbon Measurements V on the North Slope of Alaska Field Campaign ReportRep., 15 pp, DOE Office of Science Atmospheric Radiation Measurement (ARM) Program (United States).
- Boitsov, V. D., A. L. Karsakov, and A. G. Trofimov (2012), Atlantic water temperature and climate in the Barents Sea, 2000–2009, *ICES Journal of Marine Science*, 69(5), 833-840.
- Carmack, E., and F. McLaughlin (2011), Towards recognition of physical and geochemical change in Subarctic and Arctic Seas, *Progress in Oceanography*, 90(1–4), 90-104.
- Chang, R. Y.-W., et al. (2014), Methane emissions from Alaska in 2012 from CARVE airborne observations, *Proceedings of the National Academy of Sciences*, 111(47), 16694-16699.
- Clerbaux, C., et al. (2009), Monitoring of atmospheric composition using the thermal infrared IASI/MetOp sounder, *Atmospheric Chemistry and Physics*, 9, 6041-6054.
- Comiso, J. C., C. L. Parkinson, R. Gersten, and L. Stock (2008), Accelerated decline in the Arctic sea ice cover, *Geophysical Research Letters*, 35(1), L01703.
- Crevoisier, C., et al. (2014), Towards IASI-New Generation (IASI-NG): Impact of improved spectral resolution and radiometric noise on the retrieval of thermodynamic, chemistry and climate variables, *Atmospheric Measurement Techniques*, 7(12), 4367-4385.
- Gambacorta, A. (2013), The NOAA Unique CrIS/ATMS Processing System (NUCAPS): Algorithm Theoretical Basis DocumentationRep., 78 pp, NOAA, NOAA Center for Weather and Climate Predication.
- Gammelsrød, T., Ø. Leikvin, V. Lien, W. P. Budgell, H. Loeng, and W. Maslowski (2009), Mass and heat transports in the NE Barents Sea: Observations and models, *Journal of Marine Systems*, 75(1-2), 56-69.
- Gawarkiewicz, G., and A. J. Plueddemann (1995), Topographic control of thermohaline frontal structure in the Barents Sea Polar Front on the south flank of Spitsbergen Bank, *Journal of Geophysical Research: Oceans*, 100(C3), 4509-4524.
- IASI-NG (2017), IASI-NG: Innovative future instrument for studying Earth's atmosphere, edited, Centre National D'Etudes Spatiales.
- Jacob, D. J., A. J. Turner, J. D. Maasakkers, J. Sheng, K. Sun, X. Liu, K. Chance, I. Aben, J. McKeever, and C. Frankenberg (2016), Satellite observations of atmospheric methane and their value for quantifying methane emissions, *Atmospheric Chemistry Physics*, 16(22), 14371-14396.

- Kolstad, E. W. (2008), A QuikSCAT climatology of ocean surface winds in the Nordic seas: Identification of features and comparison with the NCEP/NCAR reanalysis, *Journal of Geophysical Research: Atmospheres*, 113(D11), D11106.
- Kort, E. A., C. Frankenberg, C. E. Miller, and T. Oda (2012), Space-based observations of megacity carbon dioxide, *Geophysical Research Letters*, 39(17), L17806.
- Leifer, I., and R. Patro (2002), The bubble mechanism for methane transport from the shallow seabed to the surface: A review and sensitivity study, *Continental Shelf Research*, 22(16), 2409-2428.
- Leifer, I., D. Chernykh, N. Shakhova, and I. Semiletov (2017), Sonar gas flux estimation by bubble insonification: Application to methane bubble flux from seep areas in the outer Laptev Sea, *The Cryosphere*, 11(3), 1333-1350.
- Li, S., and T. A. McClimans (1998), The effects of winds over a barotropic retrograde slope current, *Continental Shelf Research*, 18(5), 457-485.
- Lien, V. S., F. B. Vikebø, and Ø. Skagseth (2013), One mechanism contributing to co-variability of the Atlantic inflow branches to the Arctic, *Nature Communications*, 4, 1488.
- Lien, V. S., P. Schlichtholz, Ø. Skagseth, and F. B. Vikebø (2017), Wind-driven Atlantic water flow as a direct mode for reduced Barents Sea ice cover, *Journal of Climate*, 30(2), 803-812.
- Loeng, H. (1991), Features of the physical oceanographic conditions of the Barents Sea, *Polar Research*, 10(1), 5-18.
- Loeng, H., V. Ozhigin, and B. Ådlandsvik (1997), Water fluxes through the Barents Sea, *ICES Journal of Marine Science*, 54(3), 310-317.
- Maslowski, W., D. Marble, W. Walczowski, U. Schauer, J. L. Clement, and A. J. Semtner (2004), On climatological mass, heat, and salt transports through the Barents Sea and Fram Strait from a pan-Arctic coupled ice-ocean model simulation, *Journal of Geophysical Research: Oceans*, 109(C3).
- Mau, S., et al. (2017), Widespread methane seepage along the continental margin off Svalbard - from Bjørnøya to Kongsfjorden, *Scientific Reports*, 7, 42997.
- McClimans, T. A., and J. H. Nilsen (1993), Laboratory simulation of the ocean currents in the Barents sea, *Dynamics of Atmospheres and Oceans*, 19(1), 3-25.
- McClimans, T. A., B. O. Johannesseen, and J. H. Nilsen (1999), Laboratory simulation of fronts between the various water masses in the Kara Sea, paper presented at Oceanic Fronts and Related Phenomena (Konstantin Federov Memorial Symposium), Intergovernmental Oceanographic Commission (IOC) Workshop Report, UNESCO'99, Pushkin, St. Petersburg, Russia.
- McClimans, T. A., D. R. Johnson, M. Krosshavn, S. E. King, J. Carroll, and Ø. Grenness (2000), Transport processes in the Kara Sea, *Journal of Geophysical Research: Oceans*, 105(C6), 14121-14139.
- Myhre, C. L., et al. (2016), Extensive release of methane from Arctic seabed west of Svalbard during summer 2014 does not influence the atmosphere, *Geophysical Research Letters*, 43(9), 2016GL068999.
- Norwegian Petroleum Directorate (2016), Resource Report Rep., 56 pp, Norwegian Petroleum Directorate., Stavanger, Norway.
- Osterkamp, T. E. (2010), Subsea Permafrost, in *Climate and Oceans*, edited by J. H. Steele, S. A. Thorpe and K. K. Turekian, pp. 252-264, Academic Press, London UK.
- Oziel, L., J. Sirven, and J. C. Gascard (2016), The Barents Sea frontal zones and water masses variability (1980–2011), *Ocean Science*, 12(1), 169-184.

- Piechura, J., and W. Walczowski (2009), Warming of the West Spitsbergen current and sea ice North of Svalbard, *Oceanologia*, 51(2), 147-164.
- Polyak, L., S. Korsun, L. A. Febo, V. Stanovoy, T. Khusid, M. Hald, B. E. Paulsen, and D. J. Lubinski (2002), Benthic foraminiferal assemblages from the Souternh Kara Sea - A river-influenced Arctic marine environment, *The Journal of Foraminiferal Research*, 32(3), 252-273.
- Razavi, A., C. Clerbaux, C. Wespes, L. Clarisse, D. Hurtmans, S. Payan, C. Camy-Peyret, and P. F. Coheur (2009), Characterization of methane retrievals from the IASI space-borne sounder, *Atmospheric Chemistry and Physics*, 9(20), 7889-7899.
- Rekacewicz, P. (2005), Oil and gas development and seabirds colonies in the Barents Region, in *Barentswatch Atlas*, edited, UNEP/GRIDA-Arendal.
- Shakhova, N., et al. (2013), Ebullition and storm-induced methane release from the East Siberian Arctic Shelf, *Nature Geoscience*, 7, 64-70.
- Skagseth, Ø., T. Furevik, R. Ingvaldsen, H. Loeng, K. A. Mork, K. A. Orvik, and V. Ozhigin (2008), Volume and heat transports to the Arctic Ocean via the Norwegian and Barents Seas, in *Arctic-Subarctic Ocean Fluxes: Defining the Role of the Northern Seas in Climate*, edited by R. R. Dickson, J. Meincke and P. Rhines, pp. 45-64, Springer Netherlands, Dordrecht.
- Stedmon, C. A., R. M. W. Amon, A. J. Rinehart, and S. Walker (2011), The supply and characteristics of Colored Dissolved Organic Matter (CDOM) in the Arctic Ocean: Pan Arctic trends and differences, *Marine Chemistry*, 124(1), 108-118.
- Stiansen, J. E., O. Korneev, O. Titov, P. Arneberg, A. Filin, J. R. Hansen, Å. Høines, and S. Marasaev (2009), Joint Norwegian-Russian environmental status 2008. Report on the Barents Sea Ecosystem. Part II – Complete report *Rep. 1502-8828*, 375 pp, Norwegian Marine Data Center (NMDC).
- Susskind, J., C. Barnet, J. Blaisdell, L. Iredell, F. Keita, L. Kouvaris, G. Molnar, and M. Chahine (2006), Accuracy of geophysical parameters derived from Atmospheric Infrared Sounder/Advanced Microwave Sounding Unit as a function of fractional cloud cover, *Journal of Geophysical Research: Atmospheres*, 111(D9), D09S17.
- Svendsen, H., et al. (2002), The physical environment of Kongsfjorden–Krossfjorden, an Arctic fjord system in Svalbard, *Polar Research*, 21(1), 133-166.
- Vinje, T., and Å. S. Kvambekk (1991), Barents Sea drift ice characteristics, *Polar Research*, 10(1), 59-68.
- Walsh, J. E., F. Fetterer, J. Scott Stewart, and W. L. Chapman (2016), A database for depicting Arctic sea ice variations back to 1850, *Geographical Review*, 107(1), 89-107.
- Wanninkhof, R., and W. R. McGillis (1999), A cubic relationship between air-sea CO₂ exchange and wind speed, *Geophysical Research Letters*, 26(13), 1889-1892.
- Westbrook, G. K., et al. (2009), Escape of methane gas from the seabed along the West Spitsbergen continental margin, *Geophysical Research Letters*, 36.
- Westbrook, G. K., et al. (2008), Estimation of gas hydrate concentration from multi-component seismic data at sites on the continental margins of NW Svalbard and the Storegga region of Norway, *Marine and Petroleum Geology*, 25(8), 744-758.
- Whitehead, J. A., and J. Salzig (2001), Rotating channel flow: Control and upstream currents, *Geophysical & Astrophysical Fluid Dynamics*, 95(3-4), 185-226.
- Wofsy, S. C. (2011), HIAPER Pole-to-Pole Observations (HIPPO): fine-grained, global-scale measurements of climatically important atmospheric gases and aerosols, *Philosophical*

451 *Transactions of the Royal Society A: Mathematical, Physical and Engineering Sciences*,
452 369(1943), 2073-2086.

453 Worden, J., S. Kulawik, C. Frankenberg, V. Payne, K. Bowman, K. Cady-Peirara, K. Wecht, J.-E.
454 Lee, and D. Noone (2012), Profiles of CH₄, HDO, H₂O, and N₂O with improved lower
455 tropospheric vertical resolution from Aura TES radiances, *Atmospheric Measurement*
456 *Techniques*, 5, 397-411.

457 Xiong, X., C. D. Barnet, Q. Zhuang, T. Machida, C. Sweeney, and P. K. Patra (2010), Mid-upper
458 tropospheric methane in the high Northern Hemisphere: Spaceborne observations by AIRS,
459 aircraft measurements, and model simulations, *Journal of Geophysical Research:*
460 *Atmospheres*, 115(D19), D19309.

461 Xiong, X., C. Barnet, E. S. Maddy, A. Gambacorta, T. S. King, and S. C. Wofsy (2013), Mid-
462 upper tropospheric methane retrieval from IASI and its validation, *Atmospheric Measurement*
463 *Techniques*, 6(9), 2255-2265.

464 Yamamoto-Kawai, M., F. A. McLaughlin, E. C. Carmack, S. Nishino, and K. Shimada (2008),
465 Freshwater budget of the Canada Basin, Arctic Ocean, from salinity, $\delta^{18}\text{O}$, and nutrients,
466 *Journal of Geophysical Research: Oceans*, 113(C1), C01007.

467 Yurganov, L., I. Leifer, and C. Lund-Myhre (2016), Seasonal and interannual variability of
468 atmospheric methane over Arctic Ocean from satellite data, *Current Problems in Remote*
469 *Sensing of Earth from Space (Sovremennye Problemy Distantionnogo Zondirovaniya Zemli*
470 *iz Kosmosa)*, 13(2), 107-119.

471